Experimental Studies of Diffusion Doped PIN Waveguides for Integrated Silicon Photonics Circuits

A THESIS

submitted by

SREEVATSA K.R.

for the award of the degree

of

MASTER OF SCIENCE

(by Research)

DEPARTMENT OF ELECTRICAL ENGINEERING

INDIAN INSTITUTE OF TECHNOLOGY MADRAS

November 2017

THESIS CERTIFICATE

This is to certify that the thesis titled **Experimental Studies of Diffusion Doped PIN Waveguides for Integrated Silicon Photonics Circuits**, submitted by **Sreevatsa K.R.**, to the Indian Institute of Technology, Madras, for the award of the degree of **Master of Science**, is a bona fide record of the research work done by him under my supervision. The contents of this thesis, in full or in parts, have not been submitted to any other Institute or University for the award of any degree or diploma.

Dr. Bijoy Krishna Das
Research Guide
Associate Professor
Dept. of Electrical Engineering
IIT-Madras, 600 036

Place: Chennai, India

Date: Tue 28$^{\text{th}}$ Nov, 2017

"Education is a progressive discovery of our own ignorance"
"Every science begins as philosophy and ends as art"
"Inquiry is fatal to certainty"

-Will Durant

Dedicated to my Parents

ACKNOWLEDGEMENTS

गुरुर्ब्रह्मा गुरुर्विष्णु गुरुर्देवो महेश्वरः।

गुरुः साक्षात् परब्रह्मा तस्मै श्री गुरवे नमः ।।

**Guru is Brahma, Guru is Vishnu, Guru is Shiva, Guru is the god of gods.
Salutations to the adorable Guru.**

ABSTRACT

KEYWORDS: Silicon Photonics , P-I-N diode, Phase shifter, Variable optical attenuator, Photodetector, Plasma dispersion, Two photon absorption

Various designs of p-i-n diodes are widely used in integrated silicon photonic circuit for electro-optic reconfiguration, modulation and detection. The injected/depleted free carriers (electrons and holes) in the waveguide core (intrinsic region) results into a change in effective refractive index of guided mode, which is the key for an electro-optic control of silicon photonics device. Integrated optical functional devices like variable optical attenuators (VOAs), phase-shifters, switches etc. have been demonstrated earlier by integrating p-i-n diodes with silicon waveguides and operating in forward bias. On the other hand, reverse biasing across p-i-n diodes sweeps out free carriers (generated due to two-photon absorption) from the waveguide core, enabling efficient nonlinear processes such as Raman amplification, four-wave mixing, etc. So far, no unique design of a p-i-n waveguide is available for all the above mentioned applications. In this work, we have used a generic diffusion doped p-i-n diode integrated with a single-mode silicon waveguide for the demonstration of VOA, phase-shifter, and photodetector (based on two-photon absorption) in 2-μm SOI substrate. The demonstrated phase-shifter has a tuning efficiency of 0.1π rad/mA; VOA has an attenuation efficiency of 0.1 dB/mA; and photodetector has been realized with a responsivity of $\sim$10 mA/W^2, at an operating wavelength of $\lambda \sim$ 1550 nm. Though the quantum efficiency of such a photodetector is relatively low, it can be efficiently used for on-chip sensing applications.

TABLE OF CONTENTS

LIST OF TABLES

LIST OF FIGURES

ABBREVIATIONS

Acronyms

C-Band	Conventional wavelength band (1530 to 1565 nm)
L-Band	Long wavelength band (1565 to 1625 nm)
WDM	Wavelength-division-multiplexing
CMOS	Complementary Metal Oxide Semiconductor
DI	De-ionized (water)
DSO	Digital Storage Oscilloscope
DUT	Device Under Test
EDFA	Erbium Doped Fiber Amplifier
FCA	Free Carrier Absorption
FCPD	Free Carrier Plasma Dispersion
ICP	Inductively Coupled Plasma
IL	Insertion Loss
MZI	Mach-Zehnder Interferometer
PDL	Polarization Dependent Loss
PPR	Positive Photo Resist
RIE	Reactive Ion Etching
SEM	Scanning Electron Microscope
SMF	Single Mode Fiber
SOI	Silicon-On-Insulator
SMU	Source Measure Unit
TE	Transverse Electric
TM	Transverse Magnetic
TPA	Two Photon Absorption
UV	Ultra-Violet
VOA	Variable Optical Attenuator

Chemical Names

Al	Aluminum
Ar	Argon
CH_3COOH	Acetic Acid
CHF_3	Tri-fluoro Methane
Cr	Chromium
HCl	Hydrochloric Acid
HF	Hydrofluoric Acid
HNO_3	Nitric Acid
H_2O	Water
H_2O_2	Hydrogen Peroxide
H_2SO_4	Sulphuric Acid
NH_4OH	Ammonium Hydroxide
SF_6	Sulfur Hexafluoride
Si	Silicon
SiO_2	Silicon dioxide
TCE	Tri-chloro Ethylene
TMAH	Tetramethylammonium Hydroxide

Units

dB	decibel
mW	milli watt
μW	micro watt
μm	micrometer
ns	nano-second
μs	micro-second
sccm	standard cubic centimeter per minute
mTorr	milli-Torr (of pressure)
mbar	milli-Bar (of pressure)
ml	milli-liter (of fluid)

NOTATION

n	Refractive index
n$_{eff}$	Effective refractive index
ϵ	Permitivity
$\boldsymbol{\lambda}$	Wavelength
$\boldsymbol{\beta}$	Propagation constant
$\boldsymbol{\beta_{TPA}}$	Two Photon Absorption coefficient
ϕ	Phase of the EM wave
L	Length (refers to device length, component length)
$\boldsymbol{\Gamma}$	Overlap integral coefficient
$\boldsymbol{\alpha}$	Loss per unit length

CHAPTER 1

Introduction

1.1 Motivation

Microelectronics industry is driven by an ever increasing requirement of high speed and energy efficient computational power. The scaling of transistor has increased speed and functionality of integrated circuits by ultra large scale integration (ULSI) of transistors. However, the metal interconnect delay [1] and the high power dissipation at these interconnects lead to performance degradation of integrated circuits [2]. These factors are motivating researchers to look at alternative solutions for mitigating the issues [3]. Silicon photonic interconnects are considered to be potential solution for inter-chip and intra-chip communication [4]. Availability of optical grade silicon-on-insulator (SOI) and established CMOS fabrication facility drives the integration of silicon electronic circuits and photonic circuits, often called marriage of electronics and photonics. Apart from the inter-chip communication using an optical interconnect, a range of applications have emerged over time. It is particular to note that short distance transceivers [5] operating at 100 Gbps are going through volume shipping for data center applications. Besides efforts to achieve high speed communications for intra systems (interconnect) and inter systems (data center applications), other fields like biosensing, biomedicine [6] have also been pursued. In addition to research in different application areas, novel device design and optimization, fabrication simplifications, development of design kits are also needed.

A single-chip silicon photonic 100 Gbps coherent transceiver [7] was demonstrated in 2014 and is shown in Figure 1.1 as an example of an integrated optical chip. The transceiver circuit has integration of various active components like p-n junction based modulator, p-i-n junction based variable optical attenuator (VOA), thermo optic phase shifter and germanium photodetector along with passive components like power splitters/combiners, polarization splitters/rotators. While all the passive components can be

directly fabricated in silicon, active components like on chip laser, thermo optic phase shifter and photodetector requires integration of other materials with silicon. While it may be necessary to integrate such components to meet desired performance for certain applications, it is also desirable to use simplified reusable designs to cut down cost and reduce fabrication complexities while compromising a little on performance. In the following section we will discuss how a p-i-n junction can be configured for phase shifting and attenuation utilizing plasma dispersion effect and for photodetection using different absorption mechanisms.
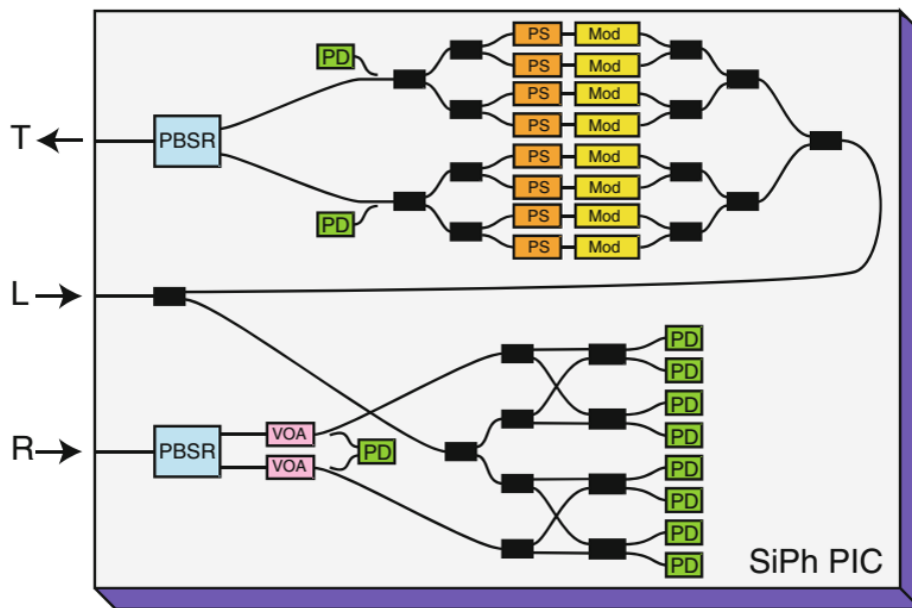
Figure 1.1: Single-chip silicon photonics 100 Gbps coherent transceiver [7].

Plasma dispersion has been one of the boons for silicon photonics. Figure 1.2 shows the schematic of three mechanisms by which free carriers can be modulated [8]. Carrier accumulation is a capacitive way of modulating free carriers where a thin dielectric material (e.g. silicon dioxide) separates the doped silicon region. Under the application of an electric field, carriers accumulate across the junction and thus refractive index is modulated. Another way of introducing free carriers is by making a lateral p-i-n junction where the intrinsic region guides light and is inherently lossless under no bias. A very good modal overlap and high level of carrier injection under forward bias can be achieved by using p-i-n junction. However, p-i-n structures cannot be operated at very high speed operation since the response time is dependent on carrier recombination lifetime. Another popular way of modulating refractive index is through a p-n junction

2
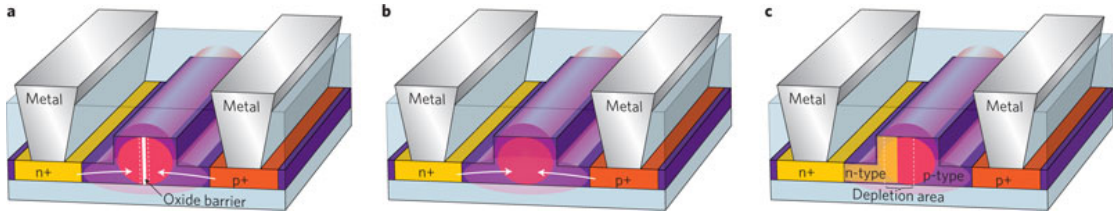
Figure 1.2: Schemes for achieving plasma dispersion effect in silicon waveguides: (a) Carrier accumulation- a thin insulating layer of silicon dioxide separates the doped silicon regions to form capacitor, (b) Carrier injection- p-i-n junction is formed by doping p and n lateral to the intrinsic waveguide core region. Under forward bias free electrons and holes are injected to the waveguide core , (c) Carrier depletion- p-n junction is formed in the waveguide core. Under reverse bias, carriers are depleted across the junction [8].

operated in reverse bias. Under reverse bias, carriers are depleted across the junction, modulation of space charge region modulates the refractive index. The modulation of free carriers is electric field driven and not through the recombination, very high speed of switching can be achieved. However, the number of carriers that can be depleted is not very high and hence the modulators utilizing carrier depletion require longer interaction lengths. A wide variety of structures have been demonstrated for improving performance like speed, power consumption and device footprint [9]. However, lateral p-n and p-i-n junctions have been the simple and effective choice for high speed modulator (p-n), phase shifter and variable optical attenuator (p-i-n).

Although silicon p-i-n diodes are used for photodetection in visible spectrum of light, at communication wavelengths (1310 nm and 1550 nm) silicon is transparent and hence photodetection is not possible. Therefore, germanium detectors are being generally integrated (by growing germanium on silicon) for on-chip detection [10]. However, precise control of germanium growth is essential to avoid defects which otherwise lead to excess optical loss and dark currents. Also, there have been efforts to make photodetectors in silicon p-i-n diodes by either implanting atoms like silicon [11], helium [12] to create defect states in the intrinsic region as shown in Figure 1.3(a) or through surface/interface states between silicon and silicon dioxide (or air cladding) interfaces [13] as shown in Figure 1.3(b). The implanted defects not only create additional optical loss but also have higher dark currents and high voltage operation in the former case and with the later, there is no way to precisely control surface states and the device operation is not reliable over time. On the other hand, as the waveguide modal areas

3
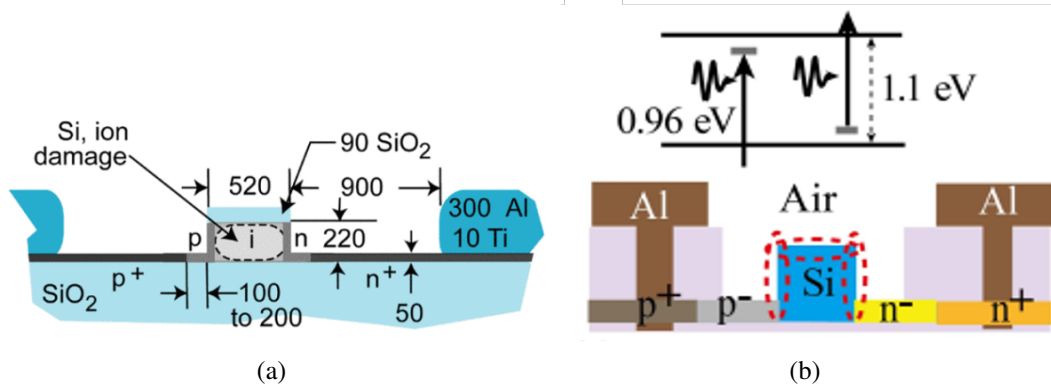
Figure 1.3: P-I-N diode integrated laterally with the waveguide with : (a) implanted intrinsic region for defect state absorption [11], (b) surface state absorption at silicon-air interface [13].

are becoming smaller in size, higher optical intensities inside the waveguide induce simultaneous absorption of two photons to generate electron-hole pairs. When the sum of energies of two photons exceed the bandgap energy, both the photons are simultaneously absorbed resulting in electron-hole pair generation. Figure 1.4 shows two cases
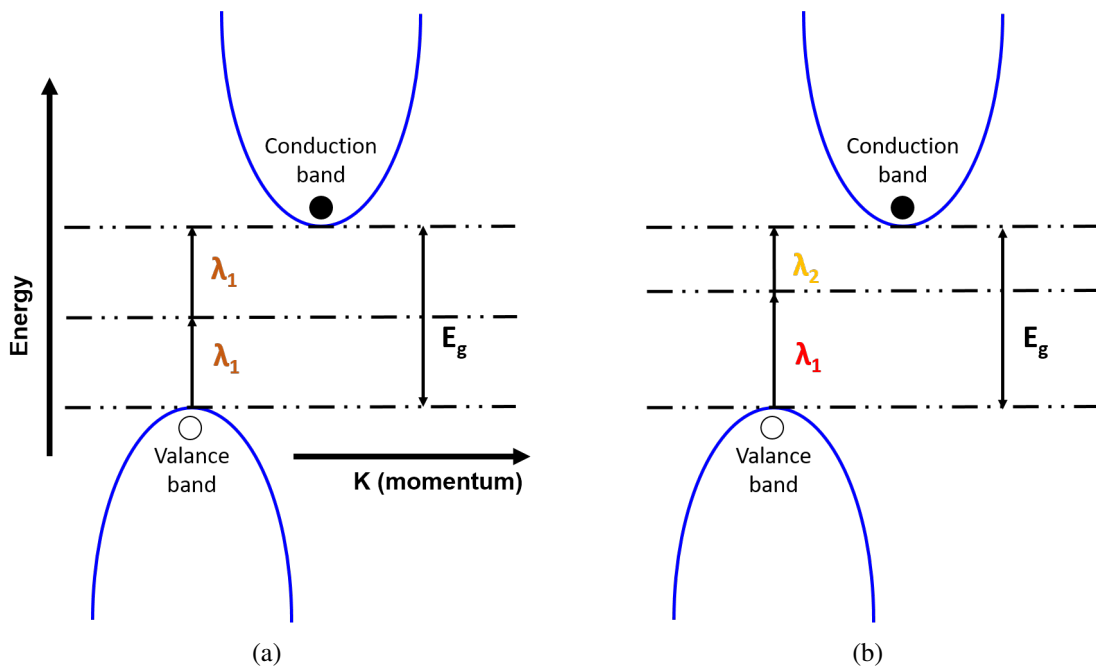
Figure 1.4: Schematic representation of two photon absorption (a) Degenerate case (two photons have same wavelength), (b) Non degenerate case (two photons have different wavelength).

of two photon absorption. Figure 1.4(a) shows the case when two photons of same energy (same wavelength) are simultaneously absorbed and Figure 1.4(b) shows a case

4

where two photons of different energy but the sum of the photon energy greater than bandgap lead to two photon absorption. The free carriers thus generated absorb light and decrease the efficiency of the nonlinear process.

While free carrier plasma dispersion by electrical injection serves as a means of electronically controlling light, free carriers generated due to two-photon absorption during nonlinear optical process deter the efficiency of the nonlinear process. Free carrier in the waveguide results in absorption of light and is detrimental in applications such as Raman amplifiers [14, 15], four-wave mixing [16], parametric generation [17] and other high power applications. However, by integrating p-i-n diodes in the waveguides, the generated carriers are removed and the performance of the device was improved [18, 19, 20, 21].

In spite of two photon absorption being an adverse effect, it has been effectively utilized in applications such as optical limiting [22], optical pulse shaping [23, 24, 25], all-optical switching and modulation [26, 27], all-optical logic gates [28, 29] and as photodetectors in various applications like pulse shape measurement [30, 31, 32], optical clock recovery [33, 34], dispersion measurements [35, 36], in-line monitoring of optical power [37, 38]. In order to minimize attenuation of optical power, free carriers need to be swept out of the waveguide core using a p-i-n diode structure. In addition to loss minimization, the photocurrent thus generated can serve as optical power monitor in an integrated photonic circuit.

1.2   Research Objective

The objective of the present work is to use a generic diffusion doped p-i-n diode integrated with a single-mode silicon waveguide for the demonstration of variable optical attenuator, phase-shifter, and photodetector (based on two-photon absorption) in SOI substrate. There was an earlier study on diffusion doped p-i-n diode integrated for Mach-Zehnder modulator in large cross section waveguides in silicon-on-insulator (SOI) with device layer of 5 μm [39] in integrated optoelectronics lab, IITM. Here we adopt same process flow for the demonstration of functionalities mentioned above in 2 - μm SOI substrate.

1.3 Thesis Organization

In chapter 2, design of single-mode waveguide, theory and simulation of plasma dispersion and two photon absorption effects in silicon waveguides are presented. The fabrication process of the p-i-n waveguide is described in chapter 3. Electro-optic characterization results of the fabricated device are discussed in chapter 4. Chapter 5 summarizes the thesis work and discuss the future scopes.

CHAPTER 2

Theory and Simulation

In this chapter, theory and simulations for waveguide design, p-i-n diode design and two photon absorption effects in the waveguide are discussed. In section 2.1, single-mode waveguide design in SOI is discussed. Section 2.2 considers the plasma dispersion effect in the waveguide which involves the the electrical simulations of the p-i-n diode and optical simulations under the influence of free carrier injection in the waveguide core. Further, the effect of free carriers generated by optical process i.e., the two photon absorption process leading to electron-hole pair generation and the effect of free carriers on light is discussed in section 2.3.

2.1   Waveguide Design

Although submicron photonic devices have compact footprint and can be densely packed, they are generally polarization dependent and dispersive. Also, light coupling in and out of these devices are difficult. On the other hand, waveguides with micron size are moderately polarization independent and dispersion free while it is also easy to package with standard fibers [40, 41, 42]. In fact, commercially available variable optical attenuators [43] and optical transceivers [44] are fabricated on 3 μm SOI substrate. Here we have used 2 μm SOI substrate for demonstration of phase shifter, VOA and photodetector.

The cross sectional view of a typical rib waveguide is shown in Figure 2.1. The top silicon is the device layer ($\sim$2 μm thick) and is selectively etched to form a rib. Silicon dioxide ($\sim$1 μm thick) below top silicon called the buried oxide acts as the bottom cladding, silicon below the oxide ($\sim$500 μm thick) is meant for handling the wafer and for mechanical strength. The top cladding for rib can be air or silicon dioxide. The waveguide width (W), slab height (h) are the design parameters that can be varied
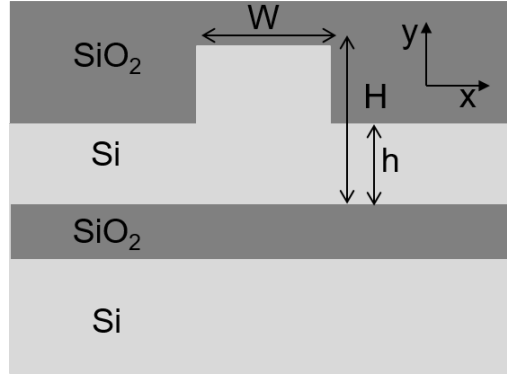
Figure 2.1: Cross-sectional view of a typical rib waveguide in SOI with silicon dioxide top cladding. H is the rib height, W is the rib width and h is the slab height.

for single-mode waveguide design. The optical modes that are supported by a given structure were calculated by solving Maxwell's equation using Lumerical Mode solver [45]. The eigen vector of the solution gives the mode profile and the eigen value gives the effective index of the guided mode. The design of a rib waveguide typically involves finding the geometry such that the structure allows single guided mode. Since the device layer height, H is fixed, the waveguide width and the slab height can be varied to find out effective index and the single-mode region of operation. Figure 2.2 shows the effective
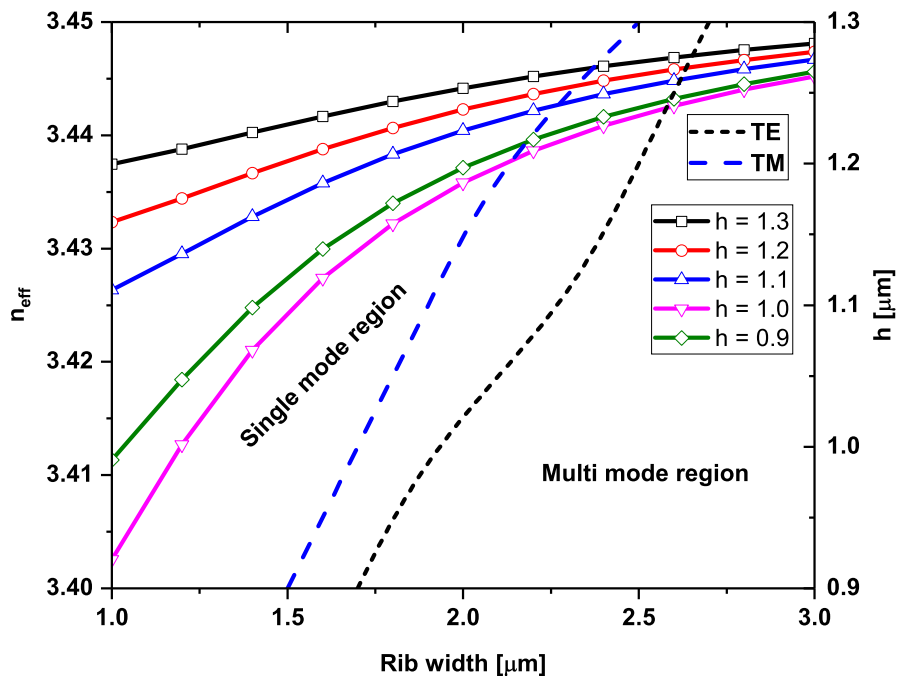
Figure 2.2: Effective refractive index of the fundamental guided mode as a function of rib width (W) (for TE polarization) for various slab heights (h). The region left to the dashed line correspond to single-mode guidance region.

index for fundamental transverse electric (TE) like mode and the single-mode cut offs for different slab heights. For a given slab height one can find out the maximum width below which the waveguide has single optical mode operation and is shown in Figure 2.2 by dashed lines for both TE and TM polarizations. The waveguide widths to the left of the dashed lines correspond to single-mode operation. A rib height of H = 1.8 μm is considered keeping in mind that some top layer of silicon will be consumed during oxidation process. The electric field profile for fundamental TE and TM polarizations is shown in Figure 2.3. The optical mode widths of fundamental TE mode corresponding

| (a) | (b) |
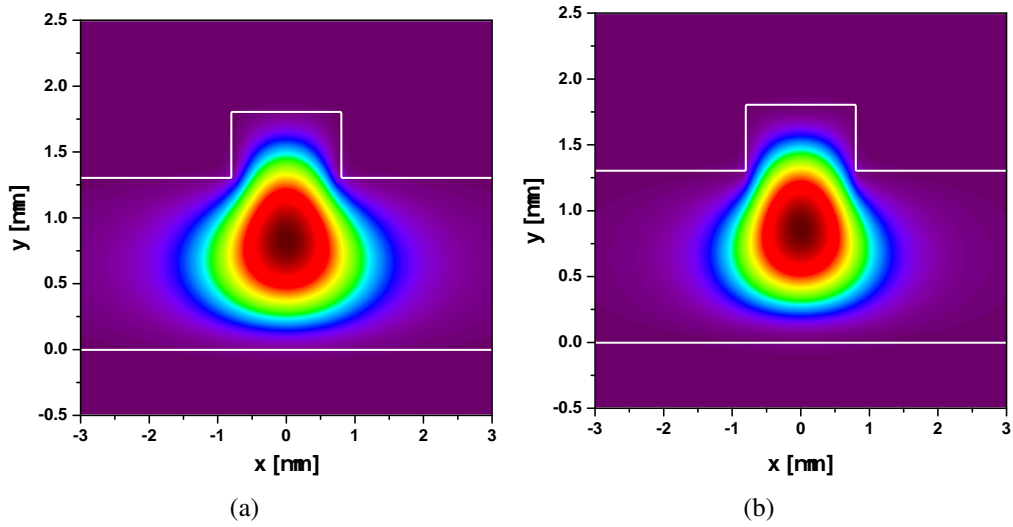
Figure 2.3: Electric field profiles for fundamental guided modes of (a) TE (E_x component) , (b) TM (E_y component) polarization for waveguide of width, W = 1.6 μm, rib height, H = 1.8 μm and slab height, h = 1.3 μm. Mode profiles calculated for a wavelength, λ = 1550 nm

to $\frac{1}{e}$ of the electric field maximum is plotted in Figure 2.4(a) and the difference in mode size between TE and TM polarization is plotted in Figure 2.4(b). Difference in mode size results in polarization dependent attenuation characteristics and is discussed in next section. Red dotted line in Figure 2.4(a) correspond to standard lens fiber mode diameter of $\sim$ 3 μm and corresponding waveguide geometry (W = 1.6 μm, H = 1.8 μm and h = 1.3 μm) is chosen for further simulation. The mode size matching is required for better modal overlap of the waveguide mode and the fiber mode which in turn helps in reducing coupling losses between fiber and waveguide.

9
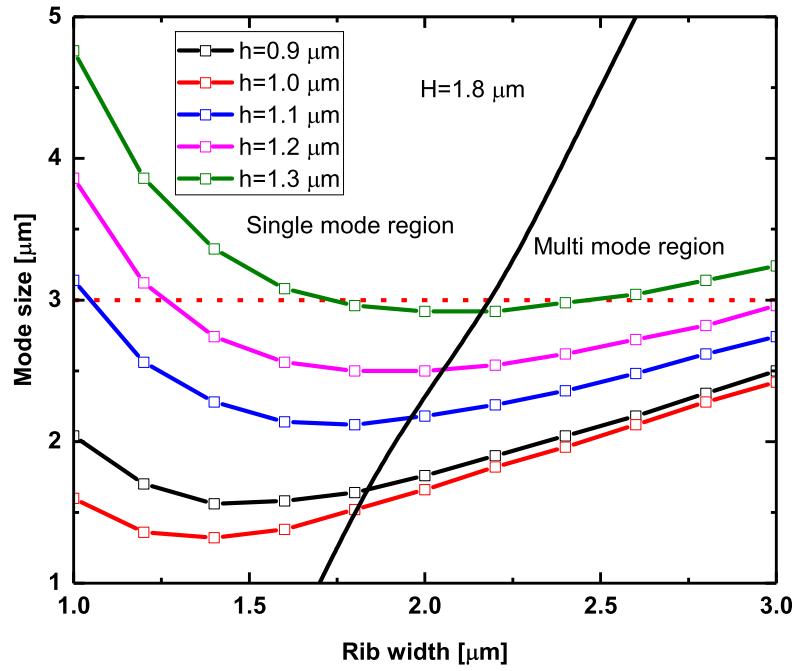
(a)
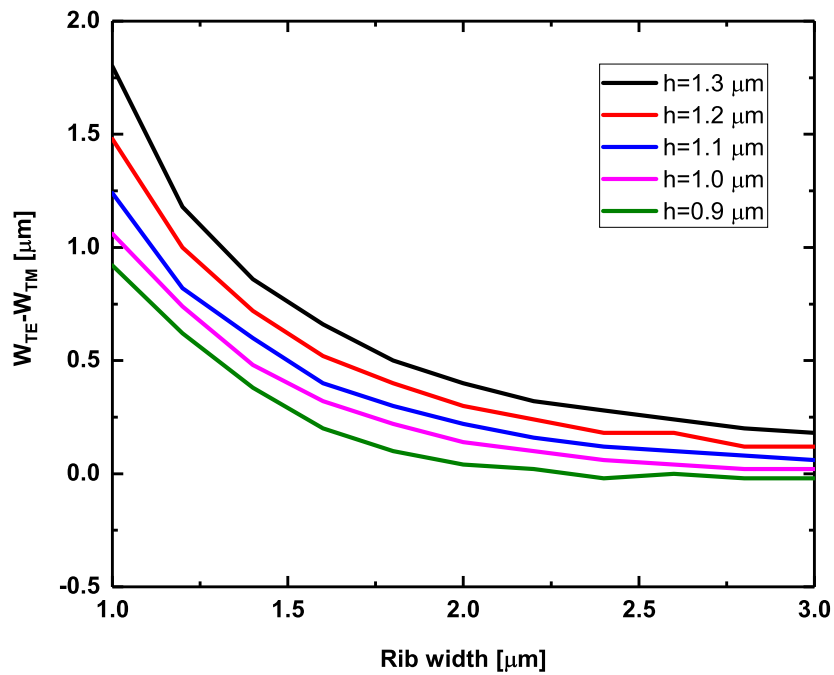
(b)

Figure 2.4: (a) Optical mode width ($\frac{1}{e}$ of maximum electric field) for TE polarization fundamental mode as a function of rib width (W) for various slab height (h). The black solid line separates single-mode and multi mode regions, red dotted line correspond to standard lens fiber mode diameter of ~ 3 μm. (b) optical mode width difference between TE and TM modes as a function of waveguide width (W) for different slab heights (h) with H=1.8 μm.

2.2 PIN Waveguide : Plasma Dispersion

After the rib waveguide geometry is designed, electro-optical simulations were carried by placing p-i-n diode. A typical p-i-n diode placed lateral to the waveguide is shown in Figure 2.5. The diode parameters that determine the electro-optic response are the doping concentration, junction depth (D_j) of the doping and the separation between the doping windows and the rib edge (S). Since the doping is carried out by diffusion process, the doping profile is assumed to be Gaussian with a surface concentration of N_s which determines the number of carriers that are injected to the waveguide core. From earlier work [39], it was observed that shallow junctions are efficient compared to a deep diffused junction. However, achieving shallow junctions with high temperature diffusion process is difficult and therefore a junction depth of 1 μm and a surface concentration of 1×10^{19} cm^{-3} for both p-type and n-type doping are assumed for simulation. The background concentration (of intrinsic region) is considered to be 10^{12} cm^{-3} in accordance with the SOI substrate specification that is used for fabrication.
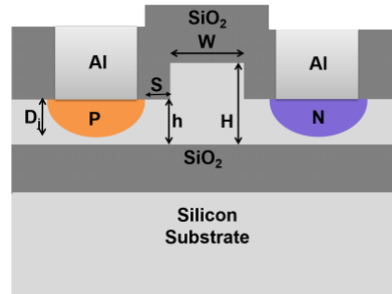
Figure 2.5: Cross-sectional view of a lateral p-i-n diode. D_j is the junction depth of the doped region p and n separated by a spacing, S from the rib edge. Waveguide core is the lightly doped intrinsic region. Aluminum contacts are for electrical probing.

The quantification of change in refractive index can be done by Drude model for free electrons. For silicon, at an operating wavelength of 1550 nm, an empirical fit is used and is given by [46] :

$$\Delta n = -[8.8 \times 10^{-22} \Delta N_e + 8.5 \times 10^{-18} \Delta N_h^{0.8}] \tag{2.1}$$

$$\Delta \alpha = [8.5 \times 10^{-18} \Delta N_e + 6.0 \times 10^{-18} \Delta N_h] \tag{2.2}$$

where, Δn and $\Delta \alpha$ (in cm^{-1}) are change in real part of refractive index and absorption (due to change in imaginary part of refractive index) because of change in electron concentration, ΔN_e and hole concentration , ΔN_h (in cm^{-3}) respectively.
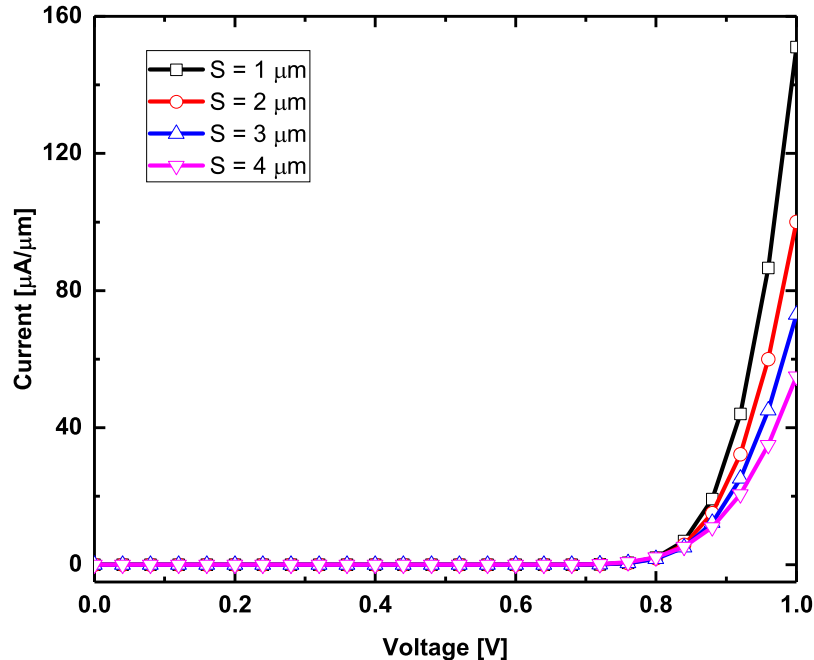
Figure 2.6: Forward bias I-V characteristics of the p-i-n diode for various doping window to rib separations (S). A junction depth of 1 μm & surface concentration of 1×10^{19} cm^{-3} (Gaussian profile) for p and n doping are assumed.

First electrical simulations are carried out in Lumerical DEVICE [47]. The simulator solves continuity equation and Poisson's equation in 2D to calculate the spatial carrier profile, electric field and I-V behavior of the diode. The carrier profile is imported into Lumerical MODE solutions [45] and the change in refractive index (both real and imaginary parts) are calculated as a function of the applied bias. The forward bias I-V characteristics of the diode for different doping window to rib separation is shown in Figure 2.6. It is obvious to expect that the diodes with narrow intrinsic region has better carrier injection compared to the wider ones. The change in real part of refractive index under forward bias is shown in Figure 2.7(a) and the attenuation due to the change in imaginary refractive index is shown in 2.7(b). A refractive index change of $\sim 1.5 \times 10^{-3}$ can be achieved around a bias voltage of around 1V and for achieving a phase change of π radians, the diode length required would be ~ 500 μm.

The separation between rib edge and doping window is an important design param-

12
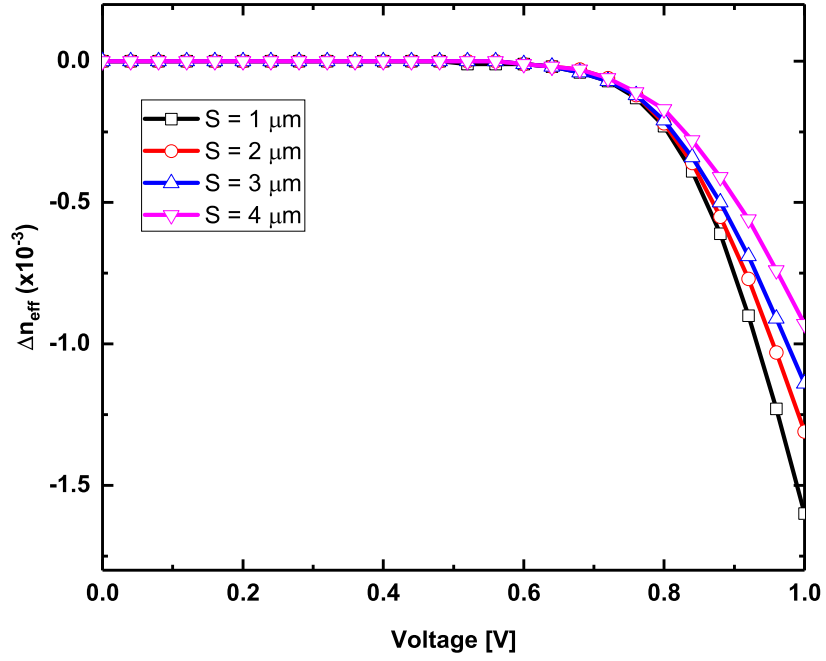
(a)
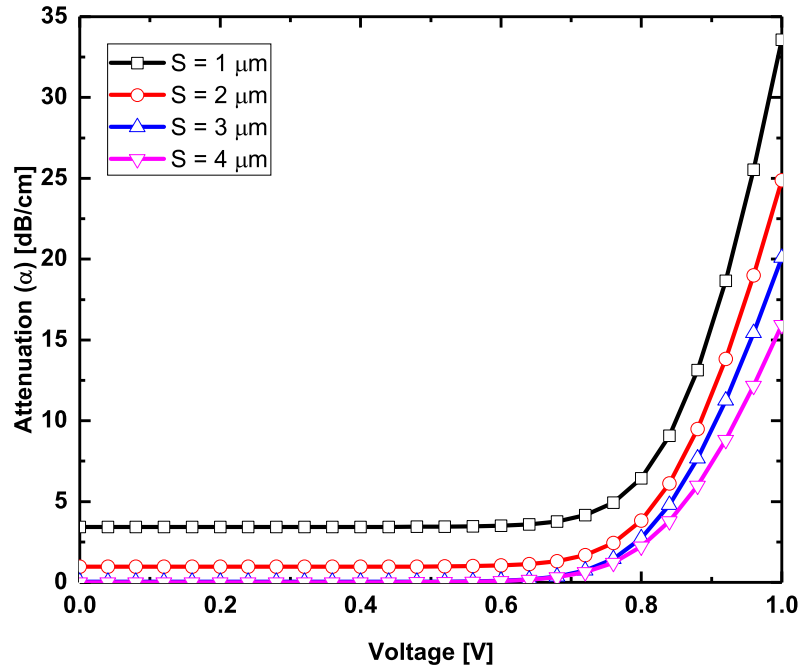
(b)

Figure 2.7: (a) Change in real part of effective refractive index (for TE polarization), (b) Attenuation due to change in imaginary part of refractive index as a function of forward bias voltage for different doping window to rib separation (S).

eter for multiple reasons. The optimum design is to ensure there is an efficient carrier injection to the core of the waveguide while not incurring additional insertion loss (IL).

First, since the doping is performed by diffusion technique, there is always lateral

13
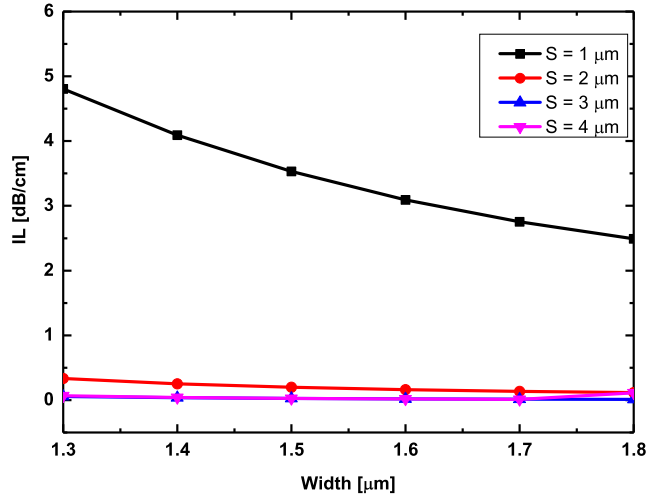
Figure 2.8: Insertion loss (loss at 0 V bias) as a function of waveguide width for different doping window to rib separation (S).

diffusion of dopant atoms which means that the waveguide will be more close to the doping regions even when the mask is at an optimum location. Secondly, from Figure 2.4(a), it can be observed that if waveguide width decreases, the mode size increases and in fact the difference in mode size between TE and TM polarization also increases as shown in Figure 2.4(b) and hence PDL also increases. This is because, when the waveguide width is reduced, the field spreads towards the slab and additional absorption of light take place. In addition to the deviation in the waveguide width, the lithographic alignment errors during opening of doping windows can also result in either additional losses if the windows align close to rib or can degrade the efficiency of carrier injection when it is away from rib. Figure 2.8 shows insertion loss when the waveguide width is varying while diodes are in fixed location. It can be observed that diodes with a separation of 1 μm suffers insertion loss greater than 3 dB for all the rib widths.

Another important figure of merit is polarization dependent loss (PDL) . PDL is defined as the difference of attenuation of TE and TM polarizations and is plotted in Figure 2.9 as a function of rib width. As it can be seen from Figure 2.3, TE like polarization has a larger mode size compared to TM like polarization. This inherently means TE mode will have more loss compared to TM mode. As waveguide width is increased, the difference between the mode size reduces, so as PDL. For a fixed rib width, smaller rib width to doping window separation has higher PDL.
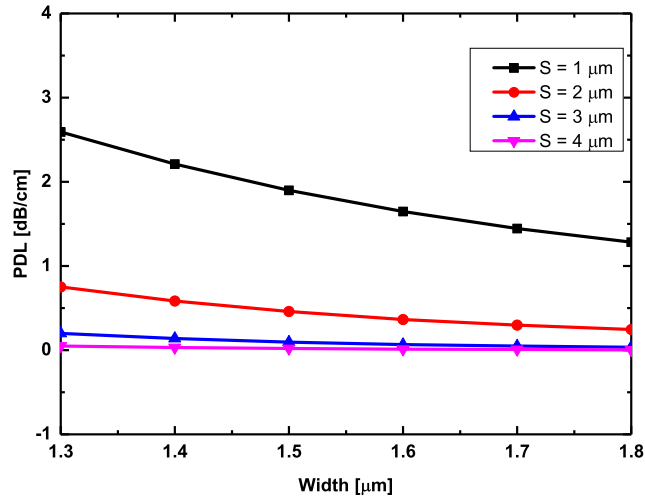
Figure 2.9: Polarization dependent loss as a function of waveguide width for different doping window to rib separation (S).
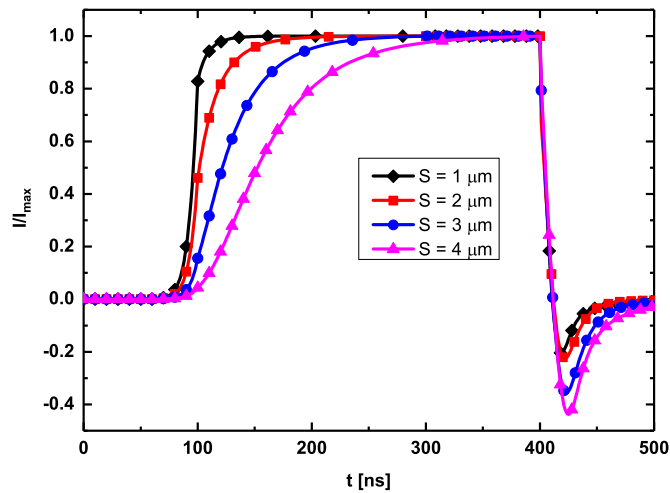
Figure 2.10: Switching response of the diode under forward bias for different doping window to rib separation (S). Input pulse has a rise time of 10 ns and computed with a step size of 1 ns.

While doping windows close to the rib creates additional losses, it has an advantage of improving the device response time. The switching response is calculated and shown in Figure 2.10 with an input pulse of rise and fall time of 10 ns. Diode with narrow intrinsic region has a faster rise time compared to wider ones. From the rise time of the step response, 3 dB electrical bandwidth can be calculated and it suggests that the p-i-n diodes could be operated at about 10 MHz when the separation is 2 μm while not adding additional optical loss. Considering all the above design parameters and the lithographic limitations, masks were designed with doping window to rib edge separation of 2, 3 and 4 μm with diode lengths of 100, 200, 500, 1000 and 5000 μm for experimental studies.

In a p-i-n rib waveguide, the lifetime of the free carrier plays an important role in the overall performance of diode as attenuator, phase shifter and a detector. In a rib waveguide structure shown in Figure 2.11, recombination of carriers happen not only in the bulk of silicon but also at the interfaces between silicon device layer and silicon dioxide bottom cladding layer and also between the silicon and top cladding layer (air or silicon dioxide). The effective carrier lifetime can be written as [48],

$$\frac{1}{\tau_{eff}} = \frac{1}{\tau_b} + \frac{WS_{bottom}}{A_{eff}} + \frac{[W + 2(H-h)]S_{top}}{A_{eff}} \tag{2.3}$$

where τ_{eff} is the effective free carrier lifetime, τ_b ($\sim 4\ \mu$s) is the bulk recombination lifetime, S_{bottom} and S_{top} are the surface recombination velocities at the top and bottom core-cladding interfaces respectively, A_{eff} is the effective modal area (defined in next section). The surface recombination velocity is a process dependent parameter and can be typically 100 cm/s [49]. In case of forward bias, when carriers are injected to
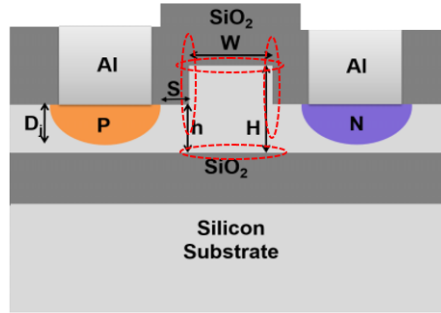
Figure 2.11: Cross-sectional view of a lateral p-i-n diode. Red dotted circles represent the interfaces where carriers recombine.

waveguide core, the change in refractive index is determined by the number of carriers that are interacting with the optical mode. When the carrier lifetime is more, for a given current number of carriers will be more and hence better efficiency can be achieved in attenuation and phase shifting. The trade-off of having longer lifetime is the reduced switching time or speed of operation. On the other hand, having a longer lifetime in case of carriers generated due to two photon absorption improves the optical detection limit of the photodetectors. In other words, even less carriers generated due to smaller optical power can be collected by the diode before they recombine at the surface.

2.3 PIN Waveguide : Two Photon Absorption

In the previous section, we have discussed carrier effects in the waveguide core when carriers are electrically injected by using a p-i-n diode. In this section we will discuss carrier injection by optical effects.

For a given waveguide, the evolution of intensity along the propagation direction in presence of linear loss, two photo absorption and free carrier absorption due to two photon absorption can be modeled using a simple differential equation as given in equation 2.4 [21, 22].

$$\frac{dI(z,t)}{dz} = -\big[\alpha_{linear} + \alpha_{FCA}\big]I(z,t) - \beta_{TPA}I^2(z,t) \tag{2.4}$$

$$\alpha_{FCA} = \sigma N \tag{2.5}$$

$$\frac{dN(z,t)}{dt} = \frac{\beta_{TPA}I^2(z,t)}{2h\nu} - \frac{N(z,t)}{\tau_{eff}} \tag{2.6}$$

where, I is the space (z-propagation direction) and time (t) dependent optical intensity, α_{linear} is the linear loss (propagation loss) of the waveguide, α_{FCA} is the free carrier absorption (FCA) loss, β_{TPA} is the two photon absorption coefficient, σ is the absorption coefficient for plasma dispersion (see equation 2.2), N is the number of electron-hole pairs generated due to two photon absorption, τ_{eff} is the effective carrier lifetime and depends on waveguide geometry and the surface quality of waveguide-cladding interface [48] , $h\nu$ (= 0.8 eV for $\lambda \sim 1.55\ \mu$m) is the photon energy. The optical intensity inside the waveguide can be written as,

$$I(z) = \frac{P(z)}{A_{eff}} \tag{2.7}$$

where, A_{eff} is the effective area of the optical mode in the waveguide and is given by:

$$A_{eff} = \frac{\big[\int\int |\vec{E}(x,y,z)|^2 dxdy\big]^2}{\int\int |\vec{E}(x,y,z)|^4 dxdy} \tag{2.8}$$

where, $\vec{E}(x,y,z)$ is the electric field strength of the guided mode. The effective modal area depends on the electric field profile which is dependent on rib waveguide geometry

like width (W), height (H) and slab height (h).

Equation 2.4 can be numerically solved under different cases. For continuous wave operation time dependence can be dropped from equations 2.4 and 2.6 and carriers can be computed under steady state condition. Table 2.1 shows the constants used in the calculation.

Table 2.1: Parameters used for solving power evolution inside waveguide.

Parameters	Values
α_{linear}	0.5 cm^{-1}
β_{TPA}	0.7 cm/GW [22]
σ	14.5×10^{-18}
hν	0.8 eV
τ_{eff}	100 ns
A$_{eff}$	1.2 μm^2 [H=1.4 μm,W=h=0.7 μm]
L	2 cm

Figure 2.12: Evolution of power inside the waveguide along propagation direction under different loss mechanisms for P(z=0) = 50 mW . Blue line includes only linear propagation loss, black line includes linear loss and two photon absorption loss, red line includes linear loss, two photon absorption loss and free carrier absorption loss due to carriers generated by two photon absorption.
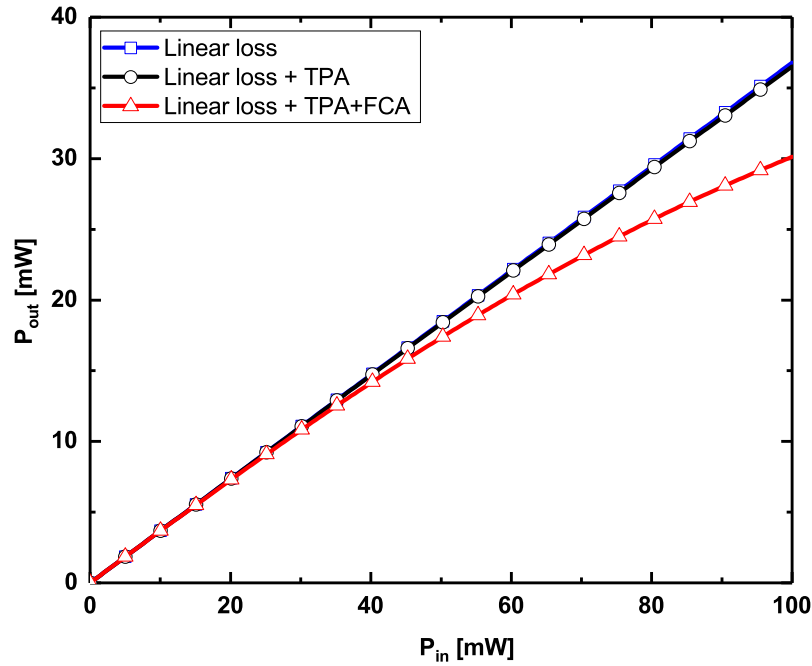
Figure 2.13: Power output considering different loss mechanisms. Blue line includes only linear propagation loss, black line includes linear loss and two photon absorption loss, red line includes linear loss, two photon absorption loss and free carrier absorption loss due to carriers generated by two photon absorption.

The evolution of optical power inside the waveguide with only linear loss, linear loss with TPA and linear loss with TPA and FCA are plotted in Figure 2.12. Input power, i.e., P(z=0) was set to 50 mW (chosen such that FCA can be distinguished). Figure 2.13 shows the the output power i.e., P(z=L) when input power is varied up to 100 mW. It is evident that for power levels up to about 40 mW, FCA is not a dominant factor and does not contribute to additional loss.

The number of free carriers generated due to TPA can be calculated along the waveguide using equation 2.6 and is shown in Figure 2.14 for various power levels. The carrier concentration is slowly varying along the length of waveguide. Therefore, if a small length is considered for fabricating a diode for photodetection, the carrier concentration can be considered as constant throughout the diode length. Longer length of the diode results in more current so that the lowest power that can be measured can be improved. Another important factor that plays a major role is the effective modal area. In a photonic wire waveguide (very small A_{eff}) high optical intensities can be achieved at low power levels as it is evident from equation 2.7. Figure 2.15 shows the through-

19

put power for various effective areas and is evident that the threshold input power level

for the on set of free carrier absorption dramatically changes for lower effective area.

Effective area can be tailored by proper choice of waveguide geometry.
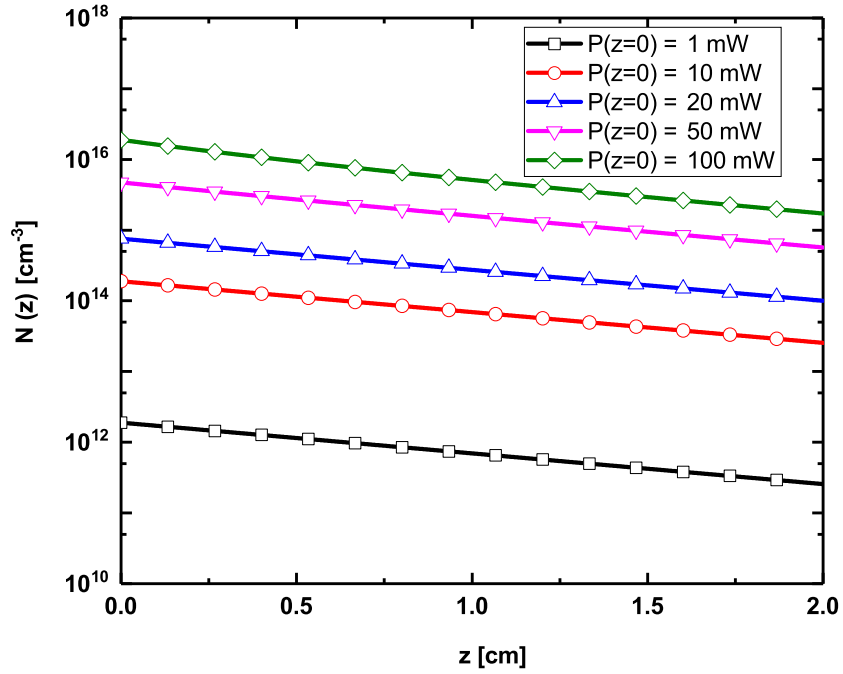
Figure 2.14: Number of electron hole pairs generated along the waveguide length at various power levels (see Table 2.1 for waveguide parameters used).
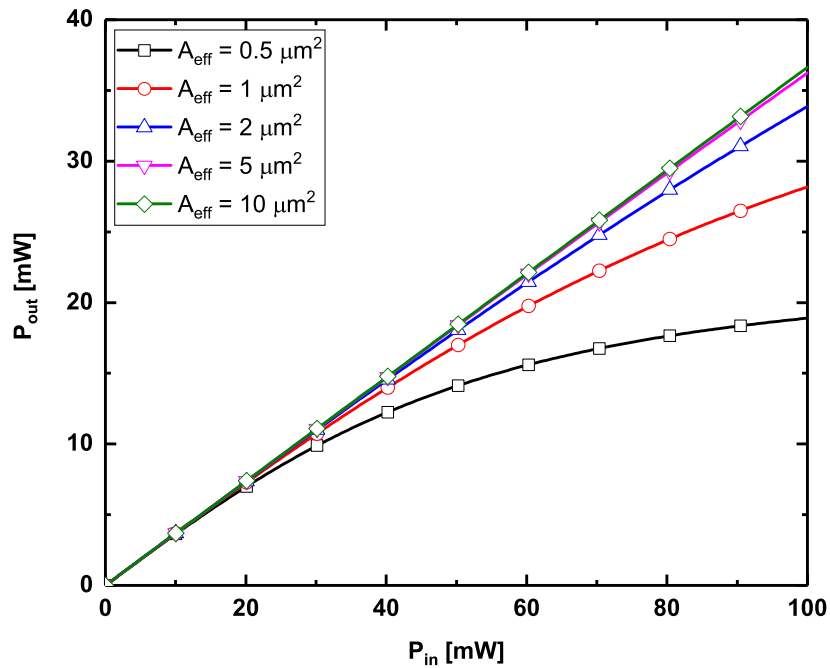
Figure 2.15: Waveguide throughput power as a function of input power for various effective modal areas (A_{eff}).

2.4   Summary

Design and simulation of p-i-n diode diodes integrated with waveguides has been carried out. First, waveguide geometry for single-mode guidance was obtained. Next, electro-optic simulations were performed to obtain the change in refractive index and optical attenuation as a function of applied bias. The change in real part of refractive index can be utilized for phase shifting application and change in imaginary part of refractive index can be utilized for electronically tunable attenuator. Placements of doping windows play an important role in design of p-i-n structures. Figure of merits like insertion loss, polarization dependent loss, response time of the p-i-n diode were calculated.

Given a waveguide geometry, the effect of two photon absorption was studied. Optical attenuation due to two photon absorption and free carrier absorption due to TPA were calculated. The carriers generated can be swept using p-i-n diode under reverse bias. Such an operation not only minimizes optical attenuation but also the resulting photocurrent can be used for on-chip detection.

CHAPTER 3

Device Fabrication

In this chapter, the process flow, mask design and process details for the fabrication of the proposed design as discussed in previous chapter are presented. The fabrication process was adopted from earlier work [39] and was slightly modified. The number of lithographic steps were reduced from 6 to 4 by choosing metal lift-off against metal etching.

3.1 Process Flow

The fabrication of waveguide integrated with p-i-n diode was carried out starting with the fabrication of waveguide first. Although silicon nitride is known to be a good diffusion mask and a passivation material as it can mask zinc, gallium, moisture and sodium which silicon dioxide cannot, due to difficulty in getting good quality silicon nitride deposition, thermally grown oxide was used as diffusion mask. Lithographically windows were opened in oxide and doping of phosphorous and boron were carried out. Metal contacts to the diode were made by first defining windows lithographically, then aluminum was deposited. Aluminum was removed from unwanted regions through lift-off technique. The cross-sectional schematic at each of the above mentioned step is depicted in Figure 3.1. The specification of the silicon-on-insulator (SOI) wafer used for fabrication is given in Table 3.1.

Table 3.1: SOI wafer specification.

Doping	p-type
Resistivity	$\sim$5 KΩ-cm
Crystal orientation	$< 100 >$
Device layer thickness	2 μm $\pm$ 0.5 μm
BOX layer thickness	1 μm
Handle wafer thickness	500 μm
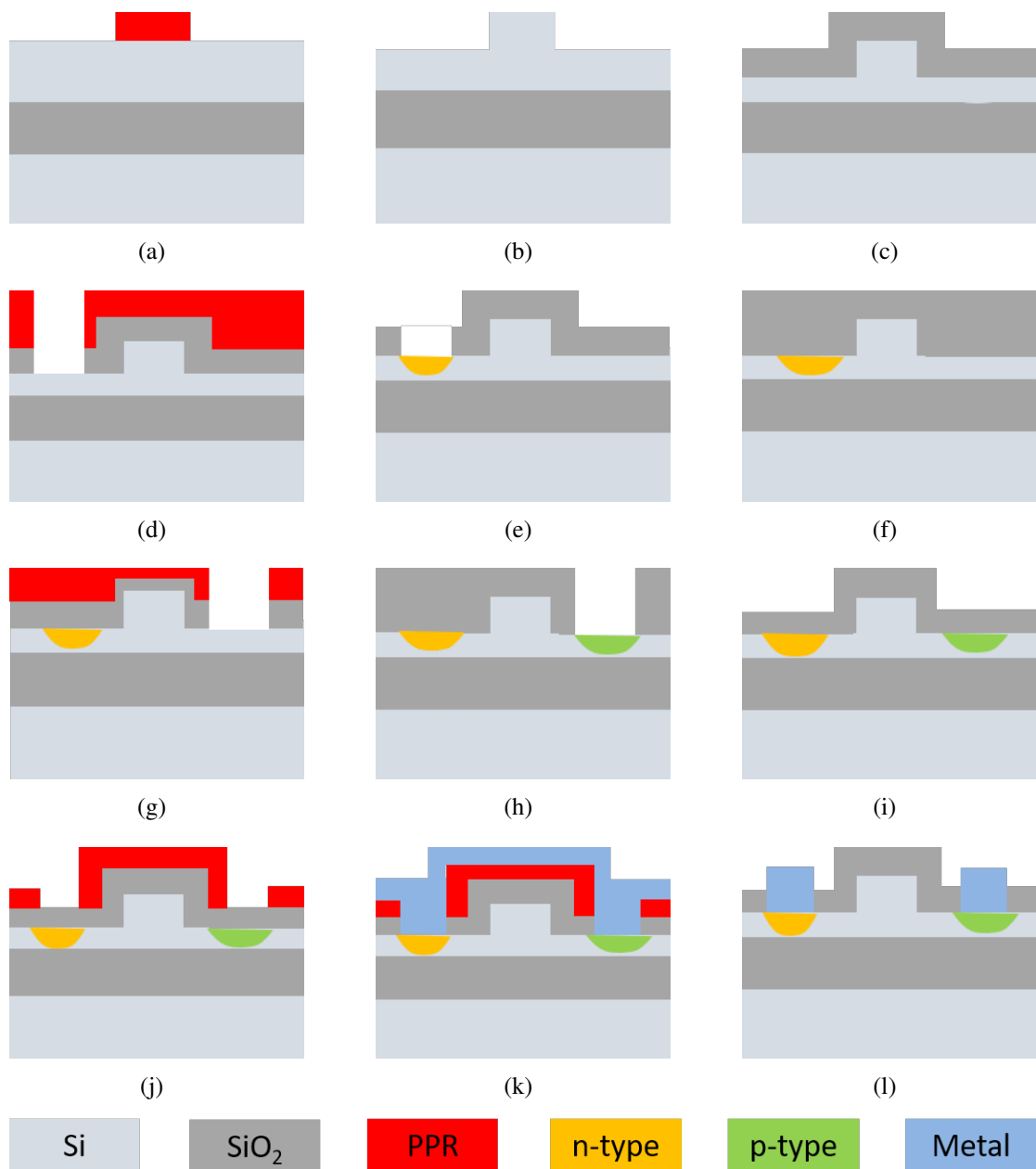
Figure 3.1: Fabrication flow and cross section of the device after (a) Photolithography for waveguide, (b) Etching, (c) Oxidation for masking diffusion, (d) Opening doping window for n-type doping, (e) Phosphorous doping, (f) Oxidation for closing doping window, (g) Opening doping window for p-type doping, (h) Boron doping, (i) Oxidation for surface passivation, (j) Opening windows for metal contacts, (k) Metal deposition, (l) Metal lift-off. (Figures not to scale)

3.2   Photomask Design and Fabrication

The fabrication of waveguide integrated with a p-i-n diode requires four lithography steps. Therefore, four masks have to be fabricated, first for the definition of waveguide, second and third for n-type and p-type doping respectively and the fourth mask for metalization. The mask layouts were designed using L-Edit CAD tool. The composite mask layout is shown in Figure 3.2. Masks were written using Heilderberg Instruments GmbH^{TM} DWL 66 mask writer (He-Cd laser of λ = 442 nm) on sodalime glass plate coated with photoresist on top of chromium. Further masks were developed in standard developer MF-319 and chromium was etched out using chromium etchant.
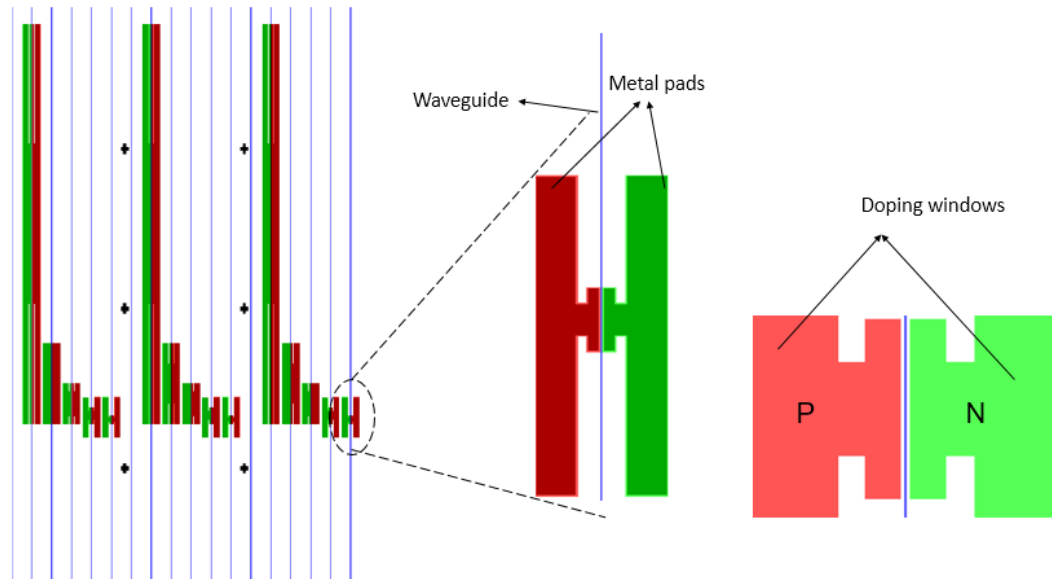
Figure 3.2: Composite mask layout including waveguide mask, p and n doping window masks, metalization mask.

3.3   Sample Preparation

Wafer Cleaning

The standard silicon cleaning procedure includes removal of organic, inorganic impurities followed by oxidation of a very thin layer of silicon and etching the same so that fresh silicon surface is available for processing. First the sample was boiled and ultrasonically agitated in trichloroethylene and acetone. The sample was rinsed in deionized

water and dried with compressed nitrogen. Then the sample was boiled in nitric acid to form a thin layer of silicon dioxide. Silicon dioxide was etched using a 1:100 mixture of hydrofluoric acid and deionized (DI) water and dried with nitrogen air. Besides the wafer cleaning at the first step, the sample needs to be cleaned before any lithography or high temperature processes. While all of the above steps may not be employed always, depending on the residue on the surface and the previous process steps, a suitable cleaning procedure was adopted. This involves cleaning with standard cleaning procedure using RCA-1 and RCA-2 solutions [50] or treatment with piranha solution (3:1 mixture of H_2SO_4 and H_2O_2). Cleaning of the sample is very critical through out the fabrication process.

Waveguide fabrication

Fabrication of waveguides was carried out in two steps. First, the waveguide patterns were transferred onto the sample from the mask photolithographically and using photoresist as mask, silicon was dry etched to a desired thickness to form rib waveguide. To transfer patterns from the mask, the sample was first spin coated (speed 3000 rpm, acceleration 450 rpm/s, time 45 second) with photoresist (S1805 - Microposit^{TM}) and baked for 20 minutes at 80 °C for removing the residual solvent of the photoresist . The sample was loaded to MA6/BA6 mask aligner and exposed with UV light (i-line, λ = 365 nm) through the photo-mask for 10 seconds. The sample was then developed using TMAH based standard developer MF-321. After development, sample was baked for 40 minutes at 80°C for hardening of photoresist which acts as mask for subsequent silicon etching. The sample was etched using inductively coupled plasma etching system (Oxford PlasmaLabSystem 100) for 40 second following a fluorine based chemistry. The details of etch recipe is tabulated in Table 3.2. Etch depth was $\sim$ 500 nm. Figure 3.4(a) shows the top view of the waveguide after etching.

Thermal Oxidation

In order to mask the diffusion doping process, thick oxide ($\sim$ 500 nm) was grown on silicon. The process was carried out after rib waveguide fabrication followed by

Table 3.2: Silicon etching recipe.

Parameters	Specifications
Gas flow rate	$SF_6 : CHF_3 :: 15 : 30$ sccm
Pressure	15 mT
Temperature	$0°C$
RF power	30 W
ICP power	1000 W
Etch rate	1 μm/minute

cleaning of the sample. The sample was loaded into the furnace at $\sim 1000°C$ in nitrogen ambient. The process of oxidation was carried out in a sequence of dry-wet-dry oxygen ambient. First dry oxidation was carried out for 15 minutes with an oxygen flow rate of 150 LPH. Then the ambient is changed to wet oxygen (steam) by passing oxygen through boiling DI water for 75 minutes. Again the ambient was changed to dry oxygen and the process was carried out for 15 minutes. Annealing of the sample was done in nitrogen ambient for 15 minutes before unloading the sample. The measured (with Ellipsometer) oxide thickness was 495 nm. The silicon dioxide thus grown acts as hard mask for diffusion processes since the diffusivity of the dopant atoms are lower in silicon dioxide compared to silicon.

Phosphorous Diffusion

The oxidized sample was patterned to open windows for doping n-type impurity. The cross-section at this step is shown in Figure 3.1(d). Then the oxide was dry etched with fluorine chemistry as given in Table 3.3. After oxide was etched, sample was cleaned and loaded into phosphorous diffusion furnace at $850°C$ in nitrogen ambient (main flow) with a flow rate of 100 LPH. Phosphorous pre-deposition was carried out for 120 minutes. Nitrogen (carrier gas) at a flow rate of 5 LPH (5% of the main N_2 flow) was bubbled through $POCl_3$ maintained in an ice bath. Oxygen (5% of the main flow) was also passed to the furnace . Nitrogen carries the vapors of $POCl_3$ and reacts with oxygen to form P_2O_5 which acts as source of doping. P_2O_5 forms a thin layer of silicon dioxide rich in phosphorous and they diffuse into silicon. The chemical reactions are

Table 3.3: Silicon dioxide etching recipe.

Parameters	Specifications
Gas flow rate	CHF_3: Ar :: 90 : 7.5 sccm
Pressure	24 mT
Temperature	20°C
RF power	200W
Etch rate	25 nm/minute

expressed as [51],

$$4POCl_3 + 3O_2 \longrightarrow 2P_2O_5 + 6Cl_2$$

$$2P_2O_5 + 5Si \longrightarrow 4P + 5SiO_2$$

The unloaded sample was dipped in 1:10 mixture of HF and DI water for about 30 seconds to remove phosphosilicate glass (PSG, an insulator) and rinsed in DI water and dried with nitrogen air. Along with the patterned sample, blank silicon samples were also loaded into the furnace so that sheet resistance could be measured. Sheet resistance was measured using four-probe method. The value of sheet resistance was 25 $\Omega/\square$ which is in close agreement to Tsuprem4 simulation 21 $\Omega/\square$ and also with the vendor data sheet [52] . The simulated doping profile is shown in 3.3(a). The junction depth was found to be 0.41 μm and surface concentration of 4×10^{20} cm^{-3}. Figure 3.3(a) also shows the profile after subsequent process steps during which there is redistribution of dopant. The expected junction depth and surface concentration at the end of all high temperature process are 1.25 μm and 1×10^{19} cm^{-3} respectively.

Boron Diffusion

Once the phosphorous diffusion was over, the doping window opened is closed by thermally growing oxide. The process conditions were same as described earlier except the process duration for dry-wet-dry oxidations were 15-30-15 minutes respectively. An oxide of $\sim$ 300 nm was grown which was sufficient for masking boron diffusion. Then windows were opened with photolithography and the cross section is shown in Figure 3.1(g) and the oxide was dry etched using the recipe as tabulated in Table 3.3. Boron nitride (BN) discs were used as solid source dopant source. First boron nitride was

soaked in a 3:2 mixture of DI water and HF for about 2 minutes and rinsed thoroughly with DI water. Since BN easily absorbs water, the discs were dried at 400 °C for 2 hours in the furnace in nitrogen ambient. Temperature of the furnace was ramped to 1000°C and oxygen is flown into the furnace at the rate of 150 LPH for 30 minutes. BN discs were unloaded to the mouth of the furnace and the temperature was further increased to 1100 °C. When the furnace has reached the set temperature, the samples were stacked alternatively with the BN discs in the quartz boat and was loaded. Diffusion was carried out for 15 minutes in an ambient of nitrogen (150 LPH) and oxygen (4.5 LPH). BN reacts with oxygen to form boron trioxide and it further oxidizes silicon to form silicon dioxide rich in boron and acts as the dopant source and boron atoms diffuse through silicon. The chemical reactions can be expressed as [51],

$$4BN + 3O_2 \longrightarrow 2B_2O_3 + 2N_2$$

$$2B_2O_3 + 3Si \longrightarrow 4B + 3SiO_2$$
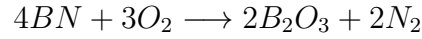
Samples were unloaded and borosilicate glass formed during diffusion was removed with HF. During the diffusion process,a silicon-boron phase is developed [53] and was removed by a subsequent step of wet oxidation at 750 °C and BSG was dissolved in HF. Sheet resistance was measured and found to be 14 $\Omega/\square$ which is in agreement with the vendor data sheet [54]. The expected junction depth and surface concentration simulated through Tsuprem4 are 1.1 μm and 1×10^{20} cm^{-3}. Figure 3.3(b) also shows the profile after surface is passivated during which there will be redistribution of impurities. The expected junction depth and surface concentration at the end of all high temperature process are 1.39 μm and 2×10^{19} cm^{-3} respectively.

Surface Passivation

After boron diffusion and low temperature oxidation, all the oxide was etched in HF and sample was cleaned. A fresh layer ($\sim$ 150 nm) of silicon dioxide was grown with dry-wet-dry oxidation for 15-10-15 minutes. This layer of oxide acts as a surface passivating layer.
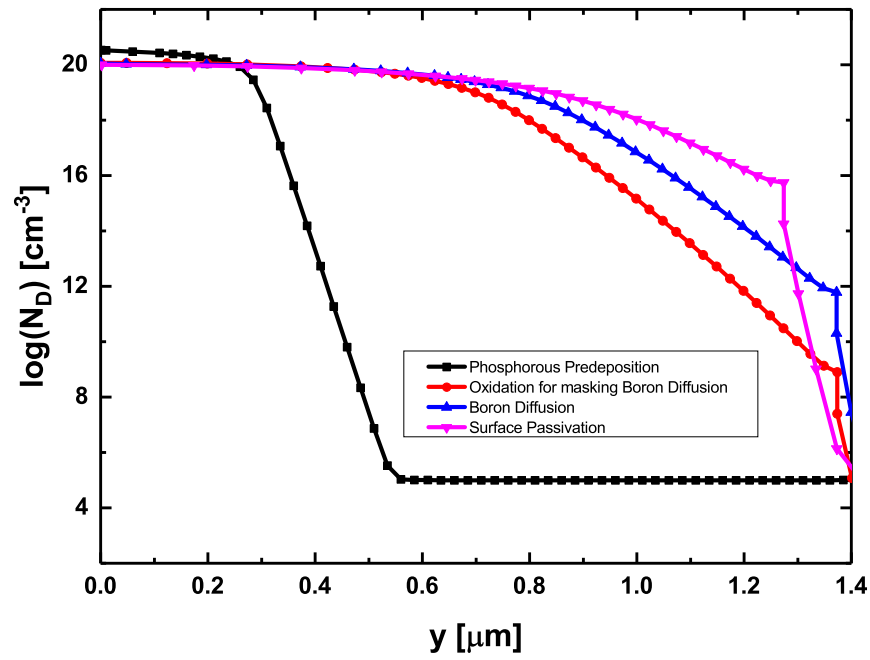
(a)
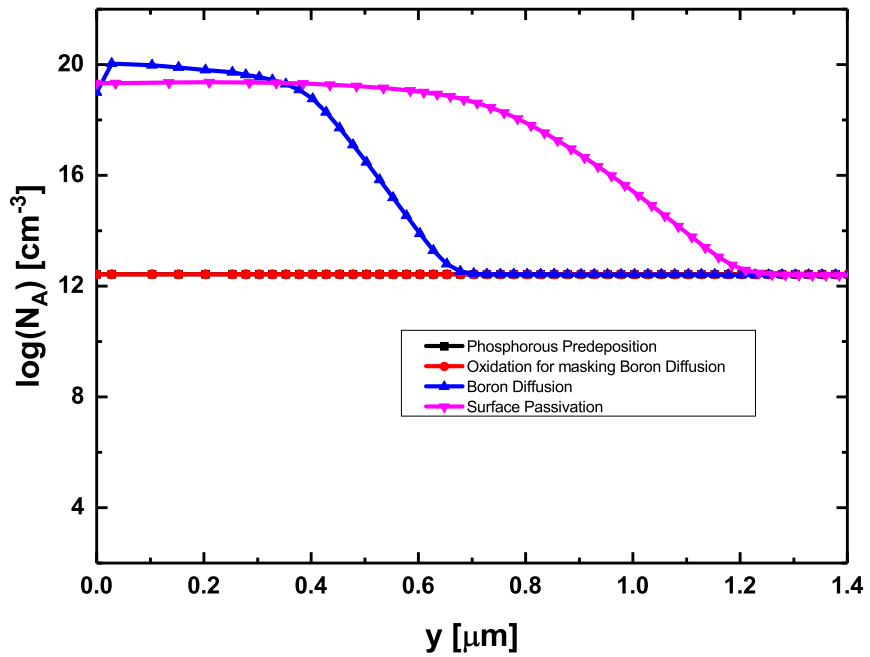
(b)

Figure 3.3: Simulated doping profile in the respective doping windows at the end of each high temperature process for (a) n-type dopant (Phosphorous), (b) p-type dopant (Boron).

Metalization

After surface was passivated, photolithographically windows were opened in oxide for making metal contacts to the p-i-n diode. Oxide was dry etched with photoresist as mask as described earlier (see Table 3.3). Figure 3.4(b) shows the top view of the waveguide along with p and n doped regions. Here it has to be noted that photoresist was not removed. Samples were then loaded to thermal evaporator and aluminum was evaporated. Aluminum thickness of $\sim$ 200 nm was deposited. Then the samples were gently agitated in acetone to lift-off metal from the un-patterned regions. The cross-sections of these processes are shown in figures 3.1(j) - 3.1(l). Figure 3.4(c) shows the top view of the sample after metalization.

(a)

(b)

(c)

(d)
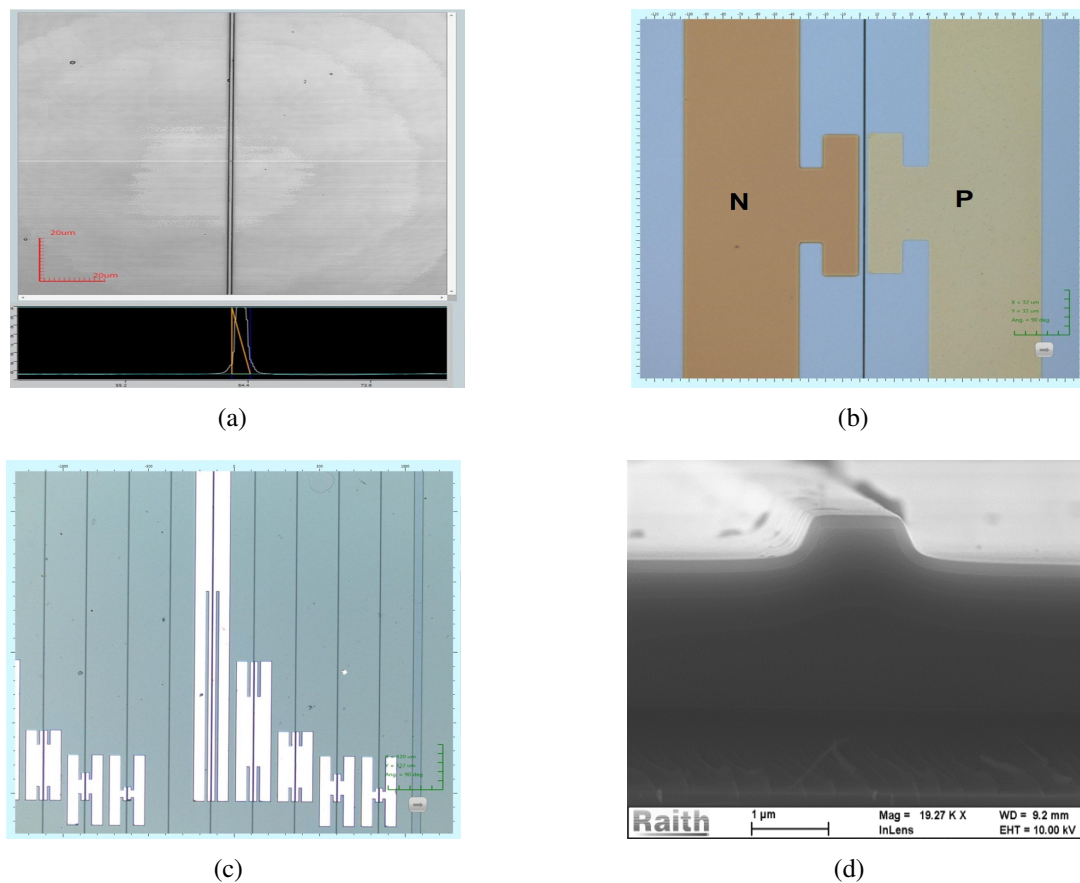
Figure 3.4: Fabricated device top-view (a) After waveguide definition, (b) After P and N doping, (c) After metalization and (d) SEM of waveguide cross-section.

End face preparation

After all the fabrication processes are completed, the end faces of the sample needs to be either polished or cleaved so that light can be coupled in/out of the waveguides. Two samples were prepared, one of them was mechanically polished using polythene films coated with diamond grains ranging from 30 μm to 0.1 μm. Polished sample was used to measure loss of the waveguide (described in next chapter). Another sample was cleaved along the cleaving plane (111). Cleaving helps in getting rid of the Fabry-Perot cavity (formed in case of polished waveguides) and helps in exact measurement of devices like variable optical attenuators. Figure 3.4(d) shows the scanned electron micro-graph of the cleaved end face.

Waveguide loss, mode profile and diode I-V measurements

Following fabrication, the waveguide losses were estimated using Fabry-Perot technique [55]. The propagation loss of the waveguides were found to be between 2-4 dB/cm for polished sample. Waveguide loss could not be measured in the cleaved sample since they do not form cavity. However, similar propagation losses are expected in the other sample. Further optical mode profiles were also measured using IR camera and typical mode profile is shown in Figure 3.5. It is clear that waveguide guides only fundamental mode. The I-V characteristics of diodes for varying doping window to rib
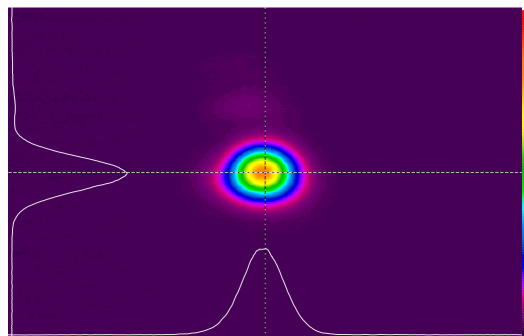
Figure 3.5: Measured optical mode profile of fundamental TE mode. (Sample #1)

separation is shown in Figure 3.6 for diode length of 500 μm. It can be seen from the diode characteristics that reverse saturation current is very low indicating good surface passivation and low defects.
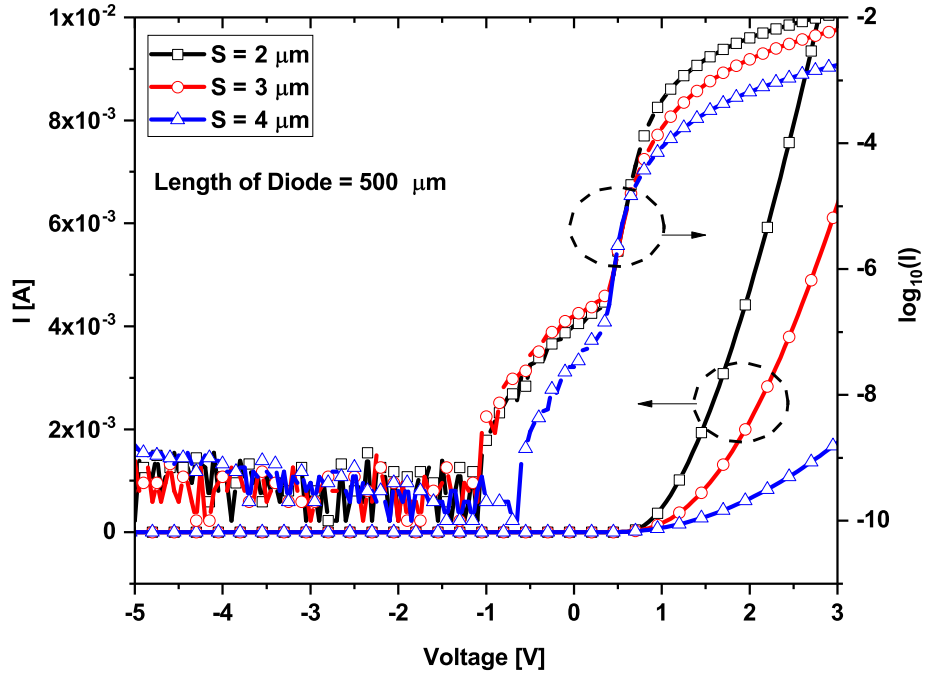
Figure 3.6: I-V characteristics of the diode for various rib to doping separation (S) for a diode length of 500 μm. Left axis is in linear scale and right axis is in log scale

3.4 Summary

Waveguide integrated with p-i-n diode is fabricated with CMOS compatible process using diffusion doping technique. Two samples were fabricated and the details of the waveguides of two samples investigated in this work are tabulated in Table 3.4. Reduced height and width in sample 2 is due to the fact that SiO_2 was removed after each diffusion processes and fresh oxide was grown before next process. The measured loss is bit

Table 3.4: Experimentally measured waveguide parameters of the fabricated samples

Parameters	Sample 1	Sample 2
Rib width (W)	1.0 μm	0.7 μm
Rib height (H)	1.8 μm	1.4 μm
Slab height (h)	1.3 μm	0.7 μm
A_{eff} (estimated)	6 μm^2	1.2 μm^2
Length	1.3 cm	1.85 cm
End-face	Cleaved	Polished
Length of diodes	100, 200, 500, 1000, 5000 μm	
Waveguide loss	–	2–4 dB/cm

higher for the fabricated waveguides. However, it would not affect the measurements of phase shifter, attenuator. Experimental results are discussed in next chapter.

32

CHAPTER 4

Experimental Results and Discussions

In this chapter optical and electrical measurement results are presented and discussed. The measurements include passive waveguide loss and mode profile measurements, active electro-optic characteristics when the p-i-n diode is in forward bias, reverse bias photocurrent measurements as a function of the input power. Also the dynamic response of the device when a square electrical signal is applied to the diodes are discussed. Two samples were prepared with slightly different waveguide dimensions (see Table 3.4). One of the samples was polished and the other sample was cleaved for end face preparation. Polished end faces forms a Fabry-Perot cavity which is useful in measuring the waveguide propagation loss and phase-shifter responses. Cleaved sample, however does not form a cavity and thus it can be used for variable optical attenuation measurements.

4.1 Experimental setup

The experimental setup used for electro-optic characterization is shown in Figure 4.1(a). Light from tunable laser source in C band (1530-1570 nm) is rotated for a particular polarization (TE or TM) and is launched to a collimating lens (10x). The collimated beam passes through a polarizer (for filtering the other polarization not of interest) and is focused onto the waveguide end face using a focusing lens (40x). Figure 4.1(b) shows the photograph of the experimental setup with sample under test between input and output objectives. The output from the waveguide is collected using a output lens (60x) and is focused on a photodetector. The output of photodetector is either connected to a power meter or digital storage oscilloscope (DSO- Keysight DSOX6002A) for steady state and dynamic measurements respectively. The electrical signal is either given from source measure unit (SMU- Keithley 2420) for DC characterization or function generator for AC characterization. All the instruments are connected to computer for control and data acquisition.
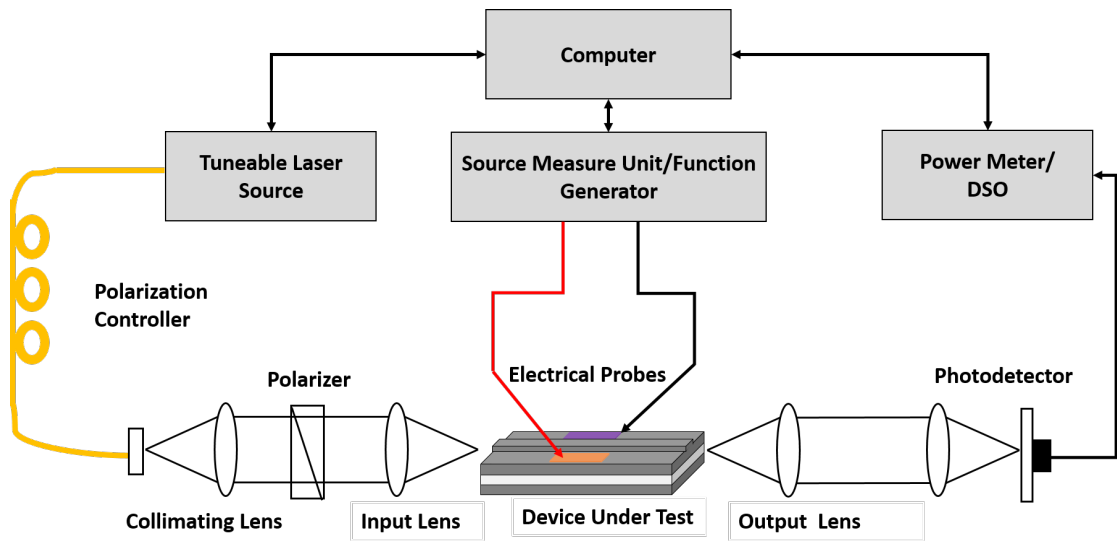
(a)
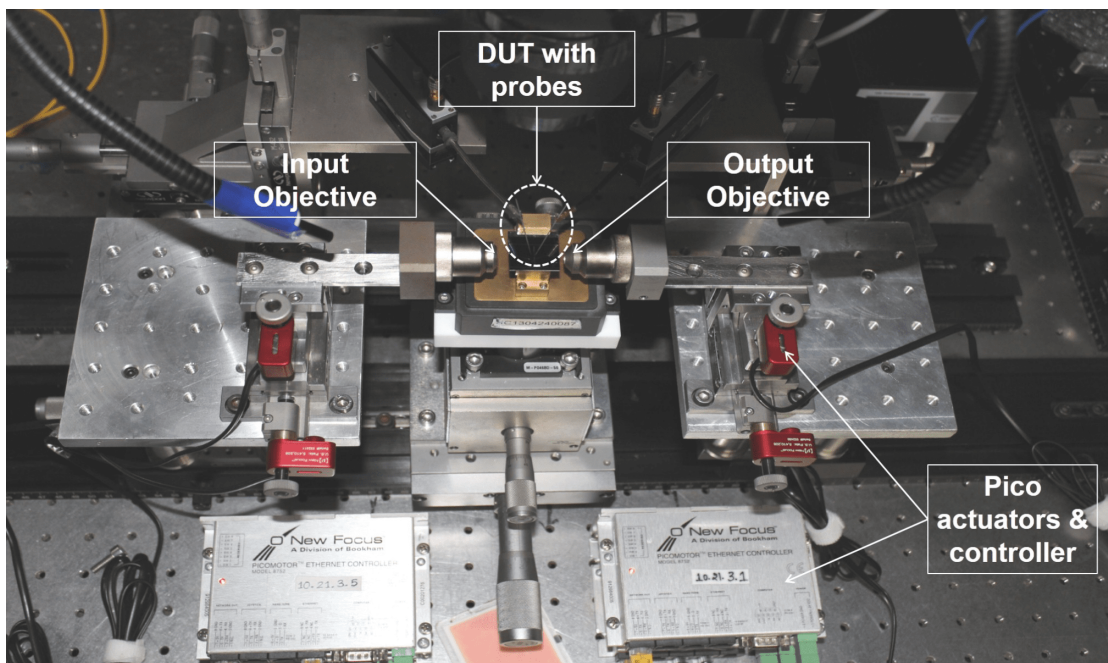
(b)

Figure 4.1: (a) Schematic of experimental setup for electro-optic characterization , (b) Photograph showing sample under test, input/output objectives and electrical probes. Pico actuators are used for precise optical alignment.

4.2   Plasma Dispersion : Phase shifter and VOA

After passive characterization of straight waveguides for loss measurements, the elec-
tro − optic characterization of the waveguides was carried out. Laser of wavelength
1550 nm was coupled to waveguides and the p-i-n diodes were electrically probed and
a forward bias was applied for injecting carriers to the waveguide core. In the fol-
lowing sections, the characteristics of phase shifter and variable optical attenuators are
discussed. As mentioned earlier, polished sample is used for measurements of phase
shifters and cleaved sample for variable optical attenuator characterization.

4.2.1   Phase shifter

Free carrier injection to the waveguide core changes both real and imaginary parts of
refractive index. In a Fabry-Perot cavity, when carriers are injected, phase modulation
results in resonances as a function of forward bias and as well attenuate the optical
power. Light of wavelength 1550 nm was coupled to waveguide using end fiber cou-
pling as shown in Figure 4.1(a). The diodes were electrically probed using micro tip
probes. Using the SMU, current is varied and optical power is monitored.
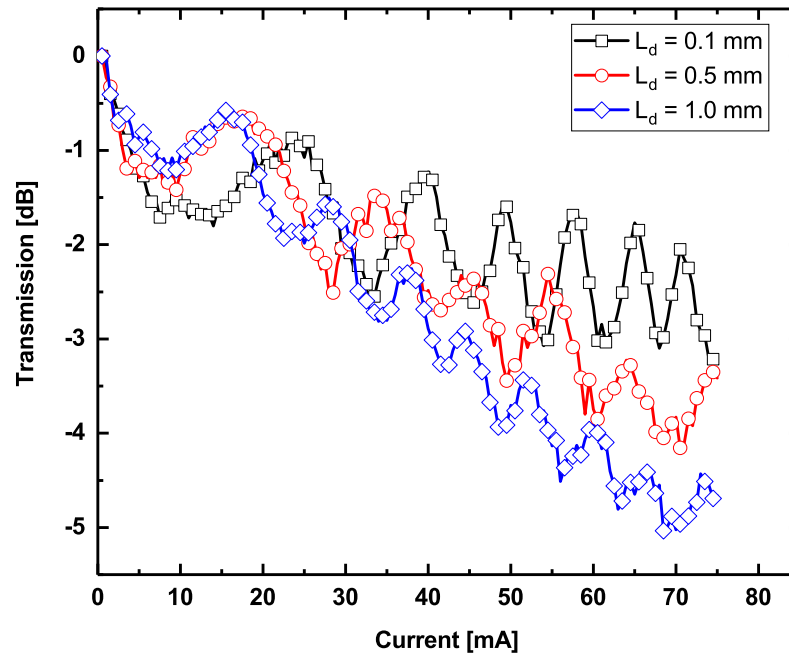
Figure 4.2: Fabry-Perot transmission under forward bias for various diode lengths (L_d).
Length of the waveguide is 1.85 cm and measured at λ = 1550 nm.

Figure 4.2 is the forward bias characteristics of the Fabry-Perot cavity for different diode lengths. The average of the transmission characteristic may be considered as the attenuation response. It is evident that longer diode undergoes more attenuation and the extinction ratio also suffers in case of longer diode length. However, shorter diode length has less attenuation and extinction ratio is nearly constant for current greater than $\sim$50 mA. If we consider an attenuation of 3 dB in a diode length of 100 μm and by assuming number of electrons and holes injected are equal, using equation 2.2, the carrier concentration can be obtained. A carrier concentration of $\sim 5 \times 10^{18}$ is required to attenuate 3 dB for a diode length of 100 μm. If we consider 5 dB of attenuation in an 1 mm diode at a forward current of 70 mA, the corresponding carrier concentration is $\sim 7 \times 10^{17}$. Since Auger recombination dominates at higher injection ($> 10^{18}$ cm^{-3}), in case of a shorter diode Auger recombination is more pronounced and hence, the net carriers available under the rib to interact with the optical mode is not increased with increase in the electrical current. Therefore, the injected current results in joule heating and the resultant Fabry-Perot modulation may be attributed to thermo-optic effect which dominates over plasma-dispersion effect in case of 100 μm diode. The maximum in the
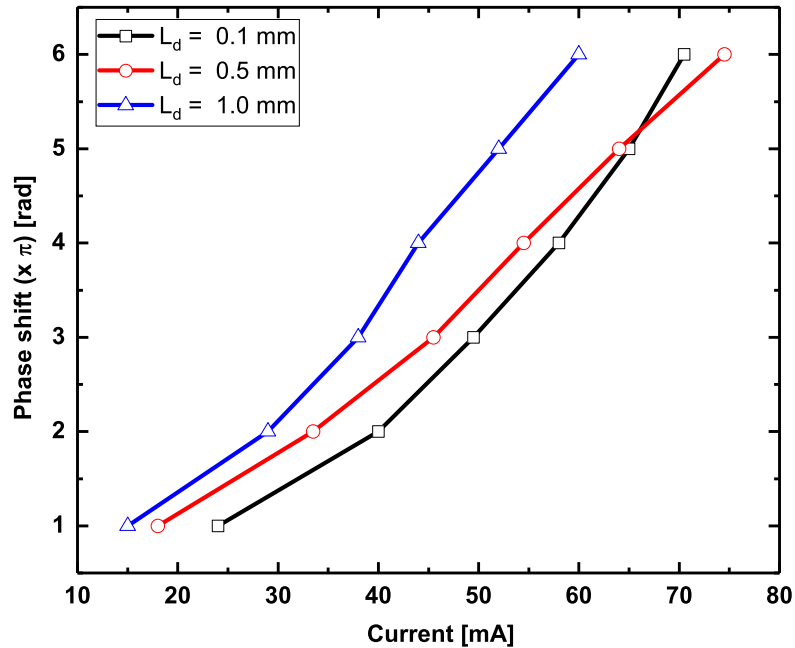
Figure 4.3: Phase shift introduced by the p-i-n diode under forward current for various diode lengths (L_d).

transmission correspond to a phase shift of integer multiples of π radians. Figure 4.3 shows the phase shift introduced by the p-i-n diode as a function of forward current. As

expected, shorter length of the diode requires higher current to attain same phase shift compared to longer diodes. By fitting the experimental points in Figure 4.3 with a linear equation, tuning efficiency can be obtained. The slope of the linear fit gives the tuning efficiency and is found to be 0.10π, 0.09π, 0.11π rad/mA for diode lengths of 5 mm, 1 mm and 0.1 mm respectively. Since the slope is independent of diode length, the values suggest that all the diodes under consideration have consistent tuning performance.

(a)

(b)

Figure 4.4: Dynamic response of the phase shifter (a) Optical signal in phase with electrical signal, (b) Optical signal out of phase with electrical signal. Yellow trace is the applied electrical signal and green trace is the optical signal. Electrical signal is at 1 MHz with rise and fall times $\sim$ 15 ns.

To measure the dynamic response of the phase shifter, the diodes were given input from a function generator with a square wave of frequency 1 MHz with rise and fall

times $\sim$ 15 ns. The output of the photodetector was connected to the oscilloscope. Figure 4.4 shows the dynamic response of the phase shifter. In Figure 4.4(a) , the modulated optical signal (green trace) is in phase with applied electrical signal (yellow trace) whereas in Figure 4.4(b) the optical signal is out of phase with respect to electrical signal. This is because of the fact that the diode is biased at a different voltage levels such that light constructively interferes when electrical signal is high in the former case and destructively in the later. The response time of the diode can be taken as the maximum of the rise and fall times and in this case it is 72 ns. It has to be noted that speed is dependent on the width of intrinsic region of the p-i-n diode. The reported response time is for an intrinsic width of $\sim$ 9 μm and diode length 1 mm.

4.2.2   Variable optical attenuator

Investigation of variable optical attenuator was carried out on the waveguides with cleaved end facets. As it does not form any cavity,the change in imaginary part of the refractive index leading to attenuation of light as a function of applied current can be measured. The attenuation characteristics for different diode lengths is shown in Figure 4.5. For the same reason as discussed earlier, Auger recombination reduces the carrier concentration in case of a shorter diode at higher forwards currents, the attenuation do not scale according to the length of the diode. The separation between doping window and waveguide rib for the above measurement was 4 μm.

The VOA characteristics for different doping window to waveguide rib separations is shown in Figure 4.6 and as expected the one with small separation results in better injection of carriers and hence better attenuation. For a fixed current value, the number of carriers that overlaps with optical mode is more when doping window is closer to rib. In other words, when intrinsic region is narrow, most of the free carriers injected interacts with light causing more attenuation. The length of the diode here is 5 mm and a maximum attenuation of 10 dB is achieved at 100 mA. Further the polarization dependency of attenuation was studied by launching light of a certain polarization with the help of polarization controller and polarizer and the results are shown in Figure 4.7 for three different gaps. It was observed that the waveguides with diodes of smaller doping win-
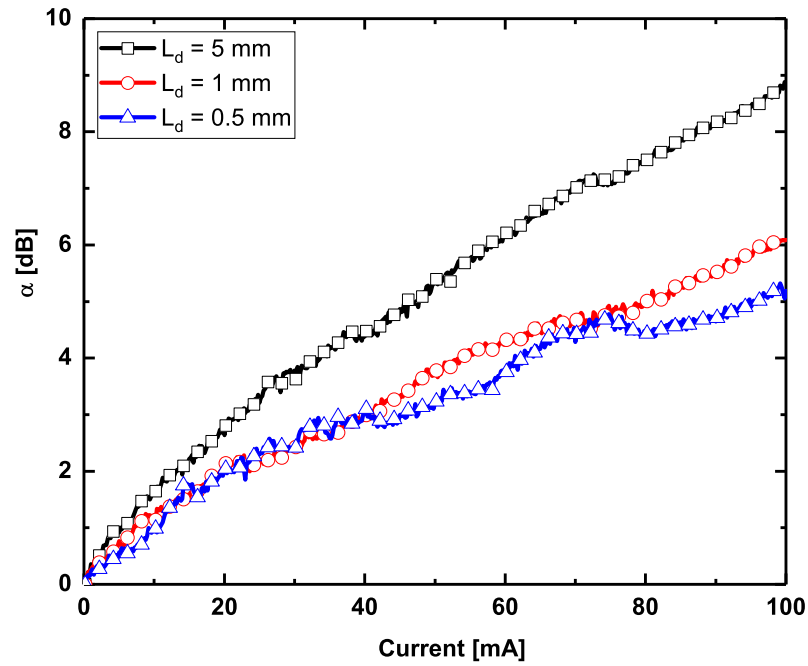
Figure 4.5: Variable optical attenuator characteristics for various diode lengths (L_d). Waveguide length is 1.3 cm, characterized with TE polarized light at λ = 1550 nm.
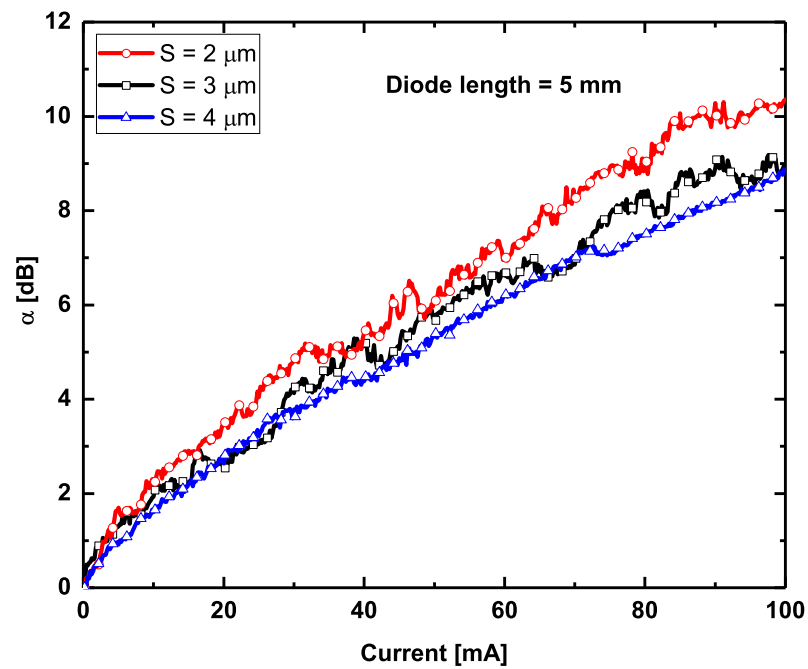
Figure 4.6: Variable optical attenuator characteristics for various diode doping window separation (S). Waveguide length is 1.3 cm, characterized with TE polarized light at λ = 1550 nm.

dow to waveguide rib separation had more polarization dependence compared to that of wider doping window to waveguide rib separation. This is due to the fact that TE like

mode will have more lateral spreading compared to a TM like mode. The optical modes for the fabricated structure was calculated and found that the $\frac{1}{e}$ width of TE like mode is ~ 5.5 μm where as for TM polarization it is ~ 4 μm. As a result TE polarization undergoes more attenuation compared to TM polarization. However, when the doping window to waveguide rib separation are wider, the carriers interaction with both the polarization are same and as a result the VOA becomes polarization independent. The measured polarization dependent loss (PDL = $\alpha_{TE} - \alpha_{TM}$) for the best device was < 0.2 dB. To study the wavelength dependency of the attenuators, wavelength was swept

(a)

(b)

(c)
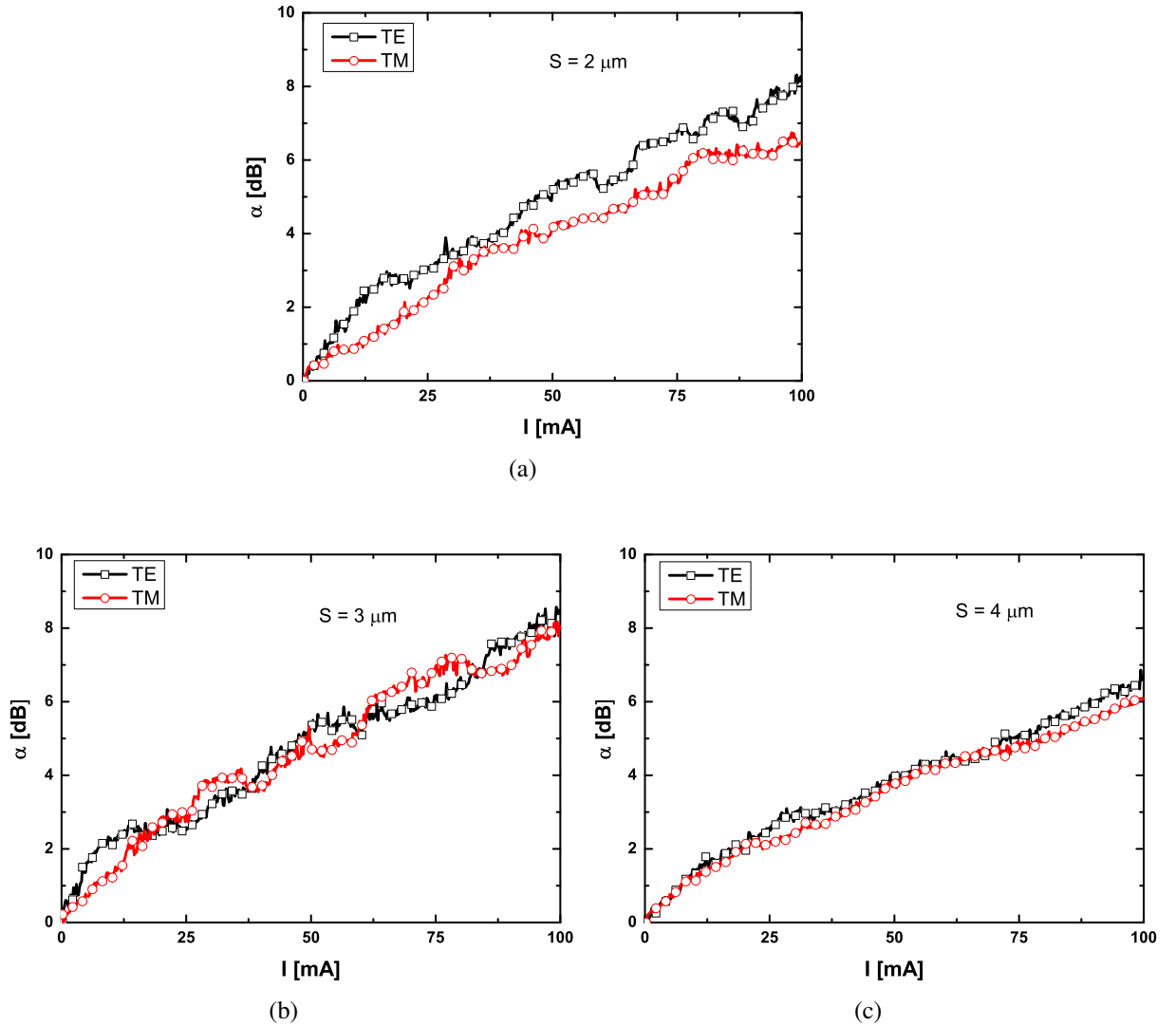
Figure 4.7: Experimental attenuation characteristics of fabricated VOAs (length = 1 mm) for both TE and TM polarizations: (a) S = 2 μm, (b) S = 3 μm, and (c) S = 4 μm.

in C-band (1530-1570 nm) while the attenuator was biased at a specific operating current. Figure 4.8(a) shows wavelength dependent characteristics for both polarizations

at different current levels. It can be seen the attenuation is nearly flat across the C-band. The standard deviation of the wavelength dependent attenuation for different devices is shown in 4.8(b) and 4.8(c). The maximum value of wavelength dependent loss is $<$ 0.5 dB. Dynamic response of VOAs were also measured with response times similar to
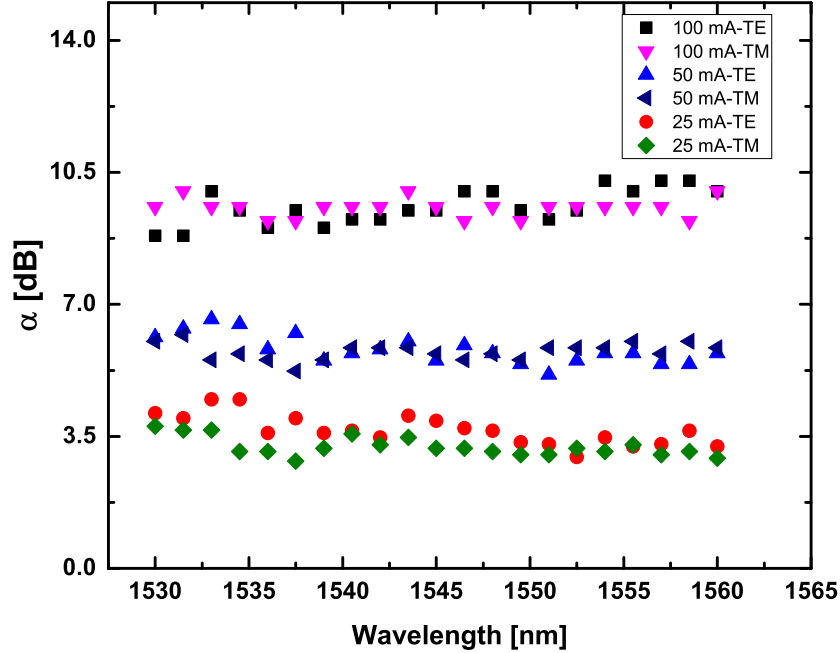
(a)
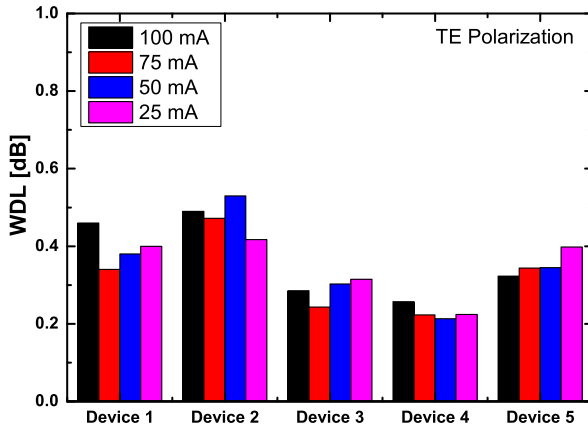
(b)
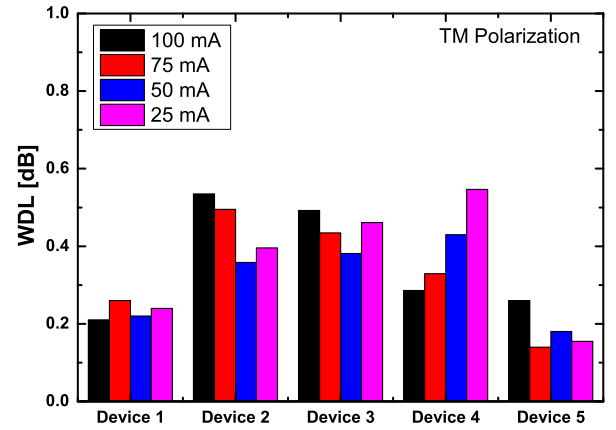
(c)

Figure 4.8: (a) Wavelength dependent attenuation characteristics, (b)–(c) Wavelength dependent loss for TE and TM polarizations respectively at different operating current levels.

phase shifters with smaller doping window to rib separation showing fast response time compared to the wider gaps. Response times were found to be 25, 65 and 125 ns for 2 μm, 3 μm and 4 μm separations respectively are consistent of simulations.

4.3 TPA : Photodetector

4.3.1 Negligible free carrier absorption

When two photons are absorbed, free carriers are generated and these carriers further absorb light and result in additional loss. The amount of loss is directly proportional to the number of carriers generated. However, if the number of carriers generated are less than $10^{17} cm^{-3}$, the additional loss is negligible compared to scattering loss. Figure 4.9 shows the loss measured at different power levels and it can be seen that there is no significant loss added by free carrier absorption. It is expected that loss should increase as power is increased. However, from Figure 4.9, it is clear that no particular trend is followed and the fluctuations is mostly due to measurement errors at different power levels. From equation 2.2 it can be calculated that for an increase in attenuation by 1 dB/cm , the number of electron-hole pairs generated to be $\sim 1.6 \times 10^{16}$ cm^{-3}. Given the length of the waveguide 1.85 cm, the number of free carriers generated is way too less to cause any attenuation.
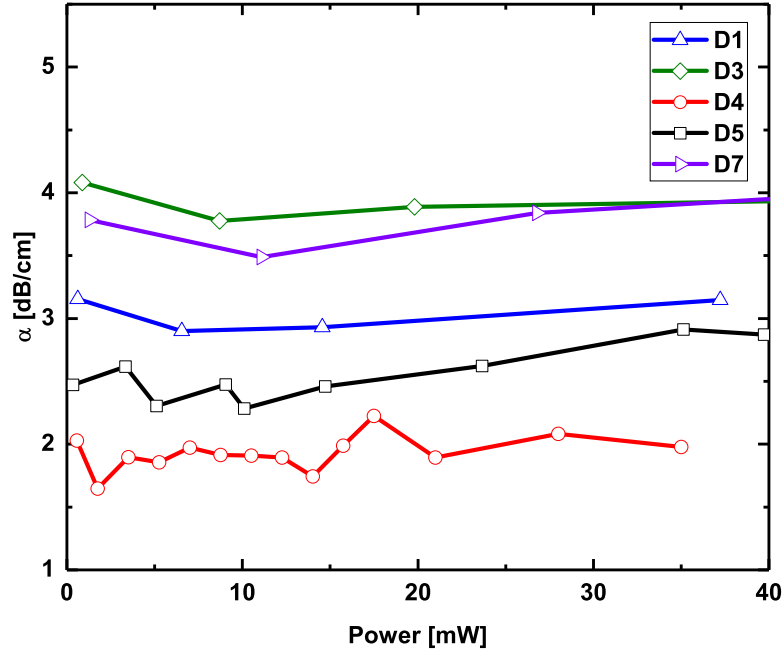
Figure 4.9: Loss measured at various input power levels for different waveguides (Device numbers: D1, D3, D4, D5, D7) at 1550 nm wavelength.

4.3.2 Photocurrent measurements and modeling

In order to measure the current due to free carriers generated by TPA, laser was tuned to 1.55 μm and light was coupled to waveguide and the p-i-n diode was probed and connected to SMU. EDFA was used to to get higher power levels for measurements. Figure 4.10 shows the reverse bias characteristics of the p-i-n diode at various power levels. It is the evident that as the power increases the reverse saturation also increases. It has to be noted that the carrier generation is quadratic with the coupled power. To measure the current as a function of power, diode was biased at a fixed voltage and the power was increased using EDFA. Photocurrent and throughput power were simultaneously recorded. Figure 4.11 shows the electric current vs optical power for different lengths of the diode. As expected longer length of the diode results in more carrier generation because of longer interaction length.
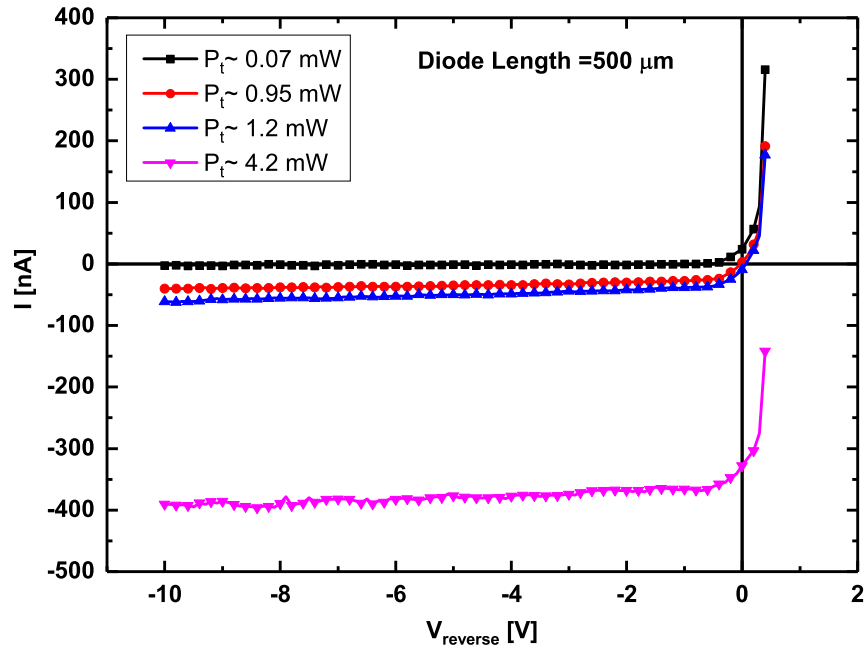
Figure 4.10: Reverse bias I-V characteristics at various power levels. Diode length, L$_d$ =500 μm.

The photocurrent was fitted with quadratic equation as given by equation 4.1.

$$I = AP_t^2 + BP_t + C \qquad (4.1)$$

$$A = \eta \frac{q\beta_{tpa}L_{eff}^{NL}}{2h\nu A_{eff}} \qquad (4.2)$$

43
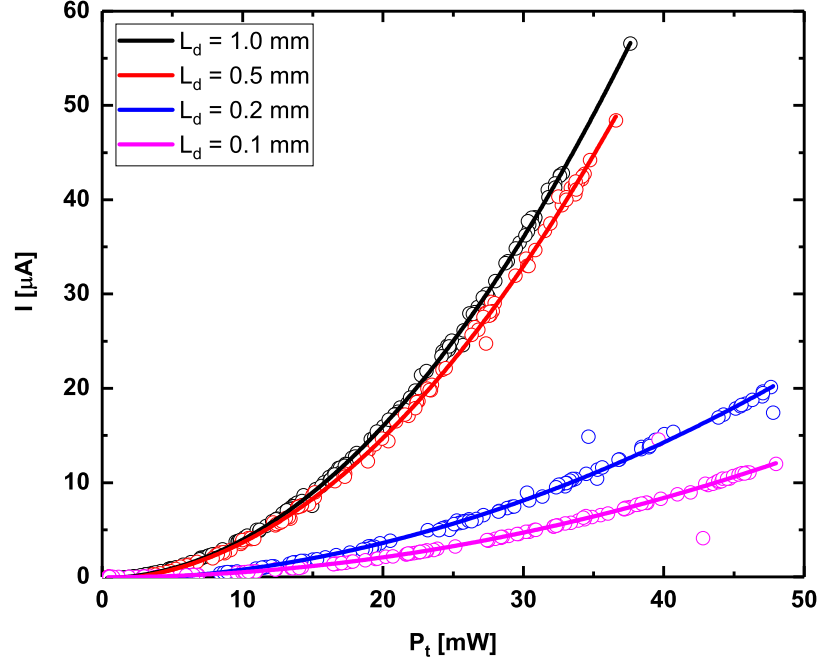
Figure 4.11: Experimental data points and quadratic fitting curves of photocurrent as a function of throughput power for various diode lengths (L_d).

$$B = \eta \frac{q \alpha_{ssa} L_{eff}^{L}}{h\nu} \tag{4.3}$$

$$L_{eff}^{NL} = \int_{l_1}^{l_2} e^{-2\alpha z} dz \tag{4.4}$$

$$L_{eff}^{L} = \int_{l_1}^{l_2} e^{-\alpha z} dz \tag{4.5}$$

where *A* (A/W^2) is considered as responsivity of the detector due to two photon absorption, *B* (A/W) is the responsivity due to surface state absorption and *C* (A) is the detector dark current. P_t is the throughput power measured using a commercial photodetector. L_{eff}^{NL} and L_{eff}^{L} are the effective interaction lengths for nonlinear and linear absorption. Since the power varies along the propagation length due to loss, effective lengths are considered for calculation. α is the propagation loss in cm^{-1}, β_{TPA} is the TPA coefficient, A$_{eff}$ is the effective modal area (~ 1.2 μm^2), l_1 and l_2 are the starting and ending points of the diode (see Figure 4.12). α_{SSA} is the surface absorption coefficient, η is the collection efficiency of the diode and is assumed to be unity. It may be appropriate to fit the equation with throughput power since it is not easy to estimate the exact coupled power to the waveguide. This results in overestimation in the values of A

and B. However, we can correct the coefficient A and B to estimate the actual responsivity. Therefore, we obtain the actual responsivity as follows. Figure 4.12 is the top
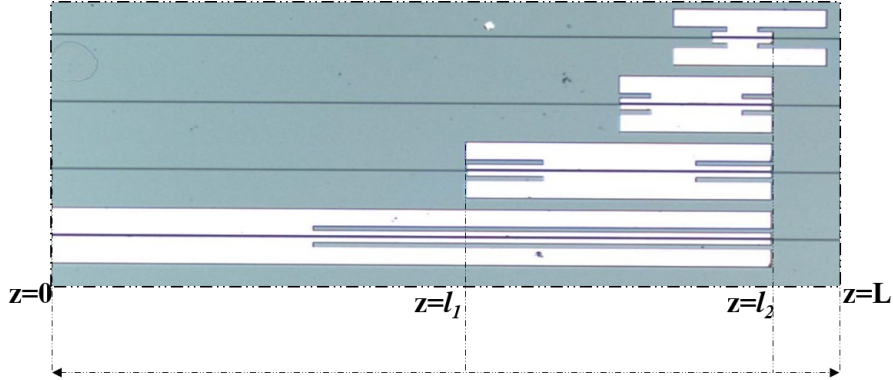
Figure 4.12: Top view of the fabricated sample showing the location of diodes. L is the total length of the waveguide. l_1 and l_2 are the starting and ending points of the diode respectively. $L_d = l_2 - l_1$ is the diode length.

view of the sample showing various diode lengths. From Figure 4.12, we can observe that location of l_2 is always fixed where as l_1, the starting point of the diode is varying for different diode lengths. The transmitted power of the waveguide of length L with a loss α can be written as,

$$P_t = P_{in}e^{-\alpha L} \tag{4.6}$$

$$P_t = P(l_1)e^{-\alpha(L-l_1)} \tag{4.7}$$

Since $P(l_1)$ is the actual power at the input of the diode and absorption starts from that point, P_t can be written as given in equation 4.7 and can be substituted in equation 4.1. Therefore, the absorption coefficient, A has to be divided by a factor of $e^{2\alpha(L-l_1)}$ and B by $e^{\alpha(L-l_1)}$ since the quadratic fitting is obtained with transmitted power and is lower than the actual power responsible for TPA.

The total length of the sample is 1.85 cm. The values of l_1, loss (α) and the coefficients (A,B,C) and the modified A $\left(A' = \frac{A}{e^{2\alpha(L-l_1)}}\right)$ are tabulated for different waveguides in Table 4.1. It has to be noted that some of the waveguides have a larger surface state absorption coefficient (e.g., device number 10) signifying a relatively poor waveguide surface and is also reflected in large dark current (C). Figure 4.13 shows the different components of photocurrent. It is clear that for power levels $> 300\ \mu$W, current due to two photon absorption is the dominant component. The quantum efficiency (Q.E) of this detector is power dependent and the magnitude of Q.E due to TPA is equal to

Device number	(l_2-l_1) (cm)	α (cm^{-1})	C (nA)	B (μA/W)	A (mA/W^2)	A$\prime$ (mA/W^2)
1	0.01	0.93	9.22	6.23	26.32	5.89
3	0.05	0.67	88.83	3.02	23.41	7.57
8	0.02	0.64	37.40	6.44	14.83	5.19
9	0.05	0.47	64.32	0.88	20.45	9.19
10	0.10	0.88	865.87	660.47	23.33	4.79
13	0.01	0.55	7.05	0.15	6.26	2.56
14	0.02	0.59	139.10	61.44	12.07	4.61
15	0.05	0.82	90.53	15.15	60.14	14.89
16	0.10	0.76	247.62	152.58	43.38	11.17

Table 4.1: Waveguide loss, diode lengths and coefficients obtained by fitting experimental photocurrent.

responsivity (coefficient A$\prime$) due to TPA. The response time of the photodetector could not be measured due to experimental limitations. However, electrical simulation of the p-i-n diode under reverse bias with an optical pulse excitation was performed and it was found that the 3 dB bandwidth is about 1 GHz.
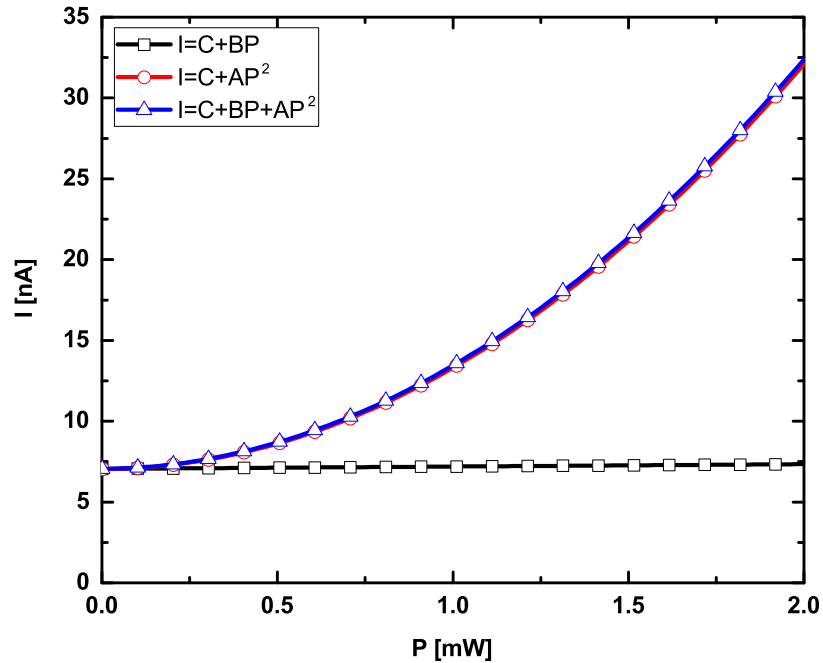
Figure 4.13: Comparison of different current components using the fitted coefficients. Black line is the current only due to linear absorption, red line is the current only due to two photon absorption, blue line is the total current.

4.3.3 Photothermal effect due to TPA

Since silicon is an indirect band gap material, electron transitions from valance band to conduction band and vice versa involves phonon generation for momentum conservation. In the process of electron-hole pair generation due to TPA, phonons are generated resulting in local increase of temperature. This effect is known as photothermal effect. As silicon has relatively large thermo-optic coefficient, refractive index will be changed due to change in temperature. It was observed that as input power is increased and output power is monitored in the polished sample, there were resonances in the transmitted power. Figure 4.14 shows the output power as a function of input power and the corresponding on-chip photocurrent measured using the p-i-n diode. The photothermal
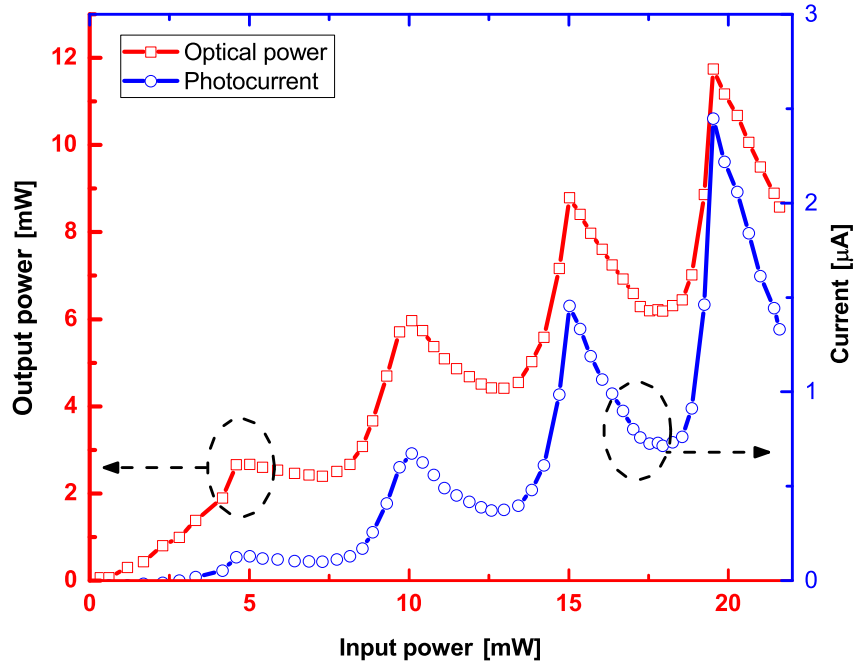
Figure 4.14: Waveguide output-input measurements. Red curve shows the optical power measured at the output of the waveguide. Blue curve shows the photocurrent measured with on-chip p-i-n diode.

effect was analyzed by calculating temperature change in the waveguide as described in [56]. The refractive index change due to temperature change, free carriers and Kerr effects as a function of power are calculated using equations 4.8 – 4.11 and is plotted in Figure 4.15.

$$\Delta T = \frac{\beta_{tpa} P_{avg}^2 \tau_t}{\rho C A_{eff}^2} \tag{4.8}$$

$$\Delta n_{thermal} = 1.86 \times 10^{-4} \Delta T \tag{4.9}$$

47

$$\Delta n_{FCD} = -(8.8 \times 10^{-22} N_e + 8.5 \times 10^{-18} N_h^{0.8}) \tag{4.10}$$

$$\Delta n_{Kerr} = \frac{n_2 P_{avg}}{A_{eff}} \tag{4.11}$$

where, ΔT is the temperature change due to carrier generation because of TPA, $\rho =$ 2.3×10^{-3} kg cm^{-3} is the density of silicon, and C = 705 J kg^{-1} K^{-1} is the thermal capacity, τ_t is the thermal diffusion time, N is the carrier generated due to TPA as defined in equation 2.6, n$_2$ = 6×10^{-18} m^2 W^{-1} is the nonlinear index coefficient, P$_{avg}$ is the average power inside the waveguide, $\Delta n_{thermal}$, Δn_{FCD}, Δn_{Kerr} are the change in refractive index due to thermal, plasma dispersion and Kerr effects respectively. The total change in refractive index is the sum of all the effects.
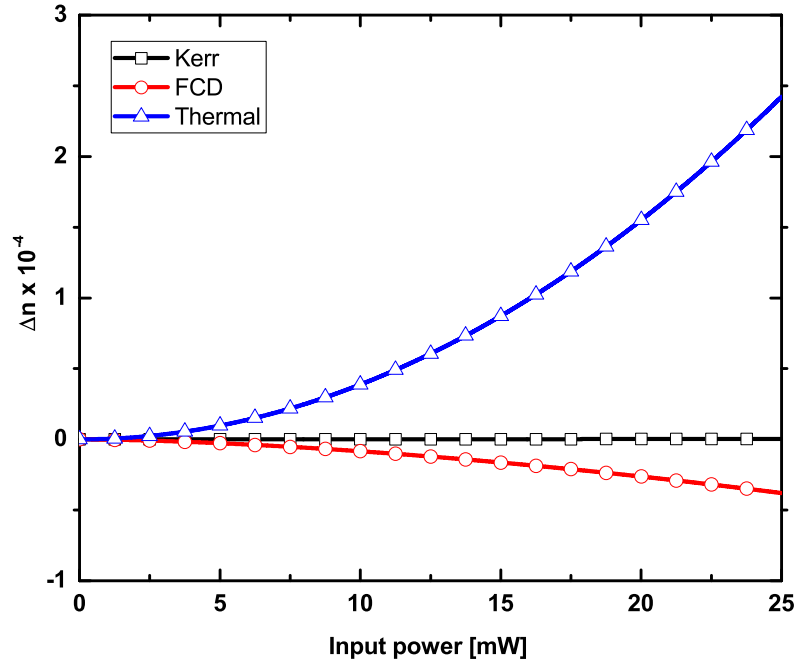
Figure 4.15: Comparison of refractive index modulation due to thermal (blue line), plasma dispersion (red line) and Kerr effect (black line) as a function of optical power.

Fabry-Perot transmission equation given by equation 4.12 [57] was used to estimate the output power by using the power dependent refractive index change.

$$P_{out} = \frac{P_{in}(1-R)^2 e^{-\alpha L}}{(1 - Re^{-\alpha L})^2 + 4Re^{-\alpha L} sin^2(\frac{\delta}{2})} \tag{4.12}$$

48

where, P_{out} and P_{in} are the output and input powers respectively, R (= 0.31) is the Fresnel reflection coefficient between silicon and air, α is the propagation loss of the waveguide, $\delta = \frac{4\pi nL}{\lambda}$ is the round trip phase shift of the cavity. Here, n is the refractive index of the mode, L is the length (in cm) of the cavity and λ is the operating wavelength.

The experimental data was fit by using thermal diffusion time constant,τ_t (about 150 μs) as fitting parameter. Figure 4.16 shows the calculated and experimental data. It has to be noted that the temperature change is less than 1°C at 15 mW of input power.
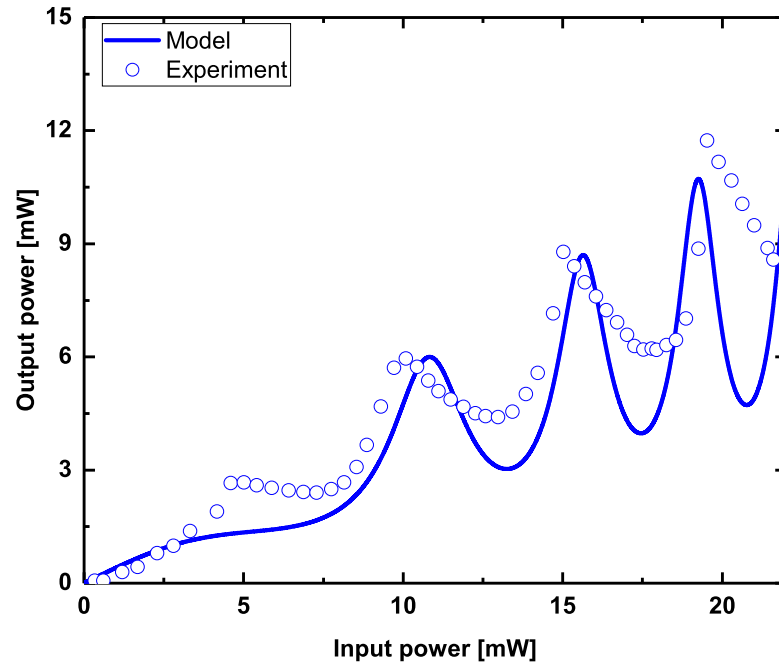
Figure 4.16: Experimental (scattered points) and theoretical model (Solid line) for waveguide input-output including thermal effects.

Further, wavelength of the laser source was tuned to measure Fabry-Perot transmission at various power levels and it was observed that the transmission peaks red-shifted at higher power levels confirming that the shift was mainly due to thermal effect.

Figure 4.17 shows the normalized power transmission at various power levels. The wavelength shift was observed to be linear with respect to power and had a slope of $\sim$ 3.2 pm/mW. Along with optical throughput, corresponding photocurrent in the on-chip p-i-n diode was also measured and is shown in Figure 4.18 and it follows the optical power.

Since the diode current follows the changes in optical power in the Fabry-Perot
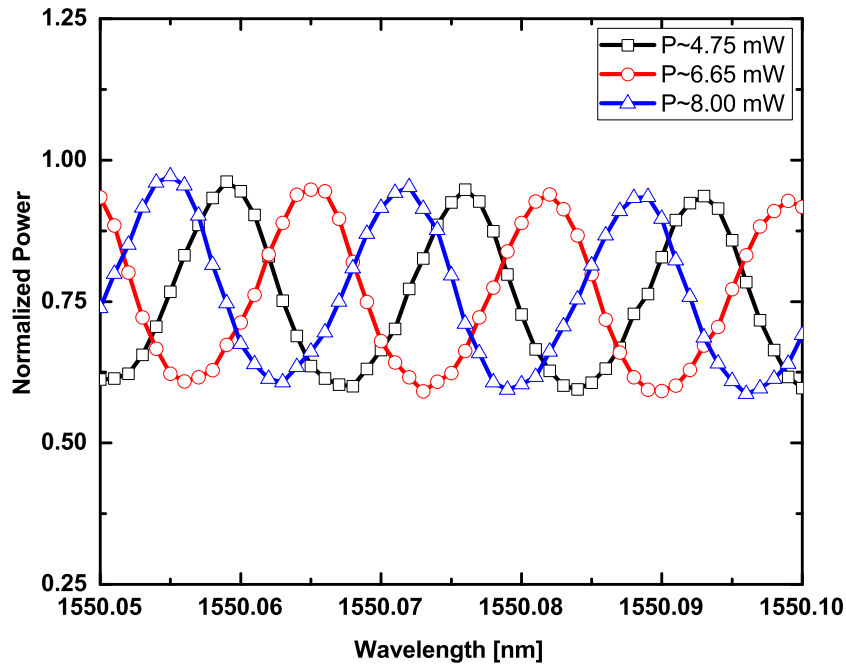
Figure 4.17: Normalized Fabry-Perot optical transmission measured at different optical power levels. Length of the waveguide is 1.85 cm, wavelength tuned with a resolution of 1 pm.
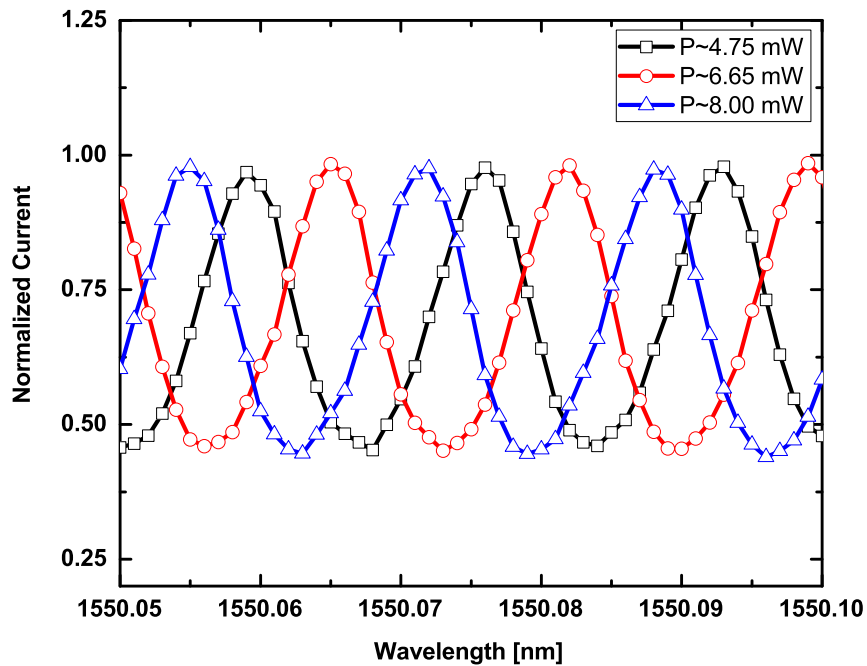
Figure 4.18: Normalized Fabry-Perot photocurrent measured at different optical power levels. Length of the p-i-n diode is 100 μm and a reverse bias of 5 V is applied for carrier sweeping.

cavity, it is possible to track down the resonance detuning by simply tracking the on-chip photocurrent and further electronics can be built into the chip for feedback control

to bring back the device in resonance condition. The sensitivity is power dependent and since the total current is quadratic, the slope (sensitivity) will be linear with power. From the product $\frac{dP}{d\lambda} \cdot \frac{dI}{dP}$, sensitivity at 5 mW of optical power is about 250 nA/pm.

In resonant devices like micro ring resonators, detuning of the resonant wavelength due to temperature or ambient fluctuations can degrade the performance of the device. A pair of p-i-n diodes may be integrated along with control circuit such that one of the diodes act as a detector and other as a phase shifter and resonance condition can be stabilized.

4.4   Summary

The fabricated devices were characterized starting with waveguide loss and mode profile measurements. Electro-optical measurements, both static and dynamic were performed to evaluate the performance of phase shifter, variable optical attenuator and photodetector. The results can be summarized as follows:

1. Straight waveguide loss were found to be 2-4 dB/cm.

2. Phase shifters have a static tuning efficiency of 0.1π rad/mA and have a dynamic response time < 100 ns.

3. Variable optical attenuators were found to be nearly polarization and wavelength independent with polarization dependent loss < 0.2 dB and wavelength dependent loss < 0.5 dB.

4. p-i-n diodes were characterized for photodetection and found to have responsivity due to two photon absorption of ~ 10 mA/W^2.

Photocurrent due to TPA and surface state absorption was analyzed using empirical models. Further, photothermal effect was observed and modeled by considering optical power dependent refractive index changes due to thermo-optic effect.

CHAPTER 5

Conclusions

5.1 Summary

In this work, we have shown that a generic p-i-n diode integrated laterally with a waveguide can be used for multiple functionalities. Such a device can be embedded at different locations of an integrated optical circuit and can be reconfigured to be used as a phase shifter, attenuator or a detector depending on the requirement. To demonstrate functionalities mentioned above, p-i-n diodes were designed, fabricated and characterized.

First, waveguides were designed for single-mode operation and with an existing set of doping parameters, diode locations was designed to achieve low insertion loss and polarization loss. The device was fabricated and characterized with electrical and optical measurements.

The experimental measurements show that phase shifter require $\sim$ 10 mA of forward current for a phase shift of π radian with a tuning efficiency of 0.1π rad/mA. The variable optical attenuator were found to be nearly wavelength independent and polarization independent (when doping window to rib separation was large) with a maximum WDL of 0.5 dB and PDL of 0.2 dB. A maximum attenuation of $\sim$ 10 dB was achieved at 100 mA of current. In terms of energy efficiency, there is of scope for improvement to reduce the power consumption by optimizing the diode design. The same diodes were operated in reverse bias for photodetection using two photon absorption. A responsivity of $\sim$ 10 mA/W^2 was measured due to TPA. As a consequence of TPA, photothermal effect in Fabry-Perot cavity was observed and was modeled by calculating the change in refractive index due to thermo-optic effect.

Although all the functionalities defined in the scope of this work are realized, there are scopes for improvement in terms of diode design, optimization of process parameters and thus improving the overall performance of the device. The waveguides losses

are on the higher side for the waveguide geometry that is considered. This can be improved by further optimizing etching chemistry. The waveguide dimensions deviate from the actual design mainly due to lithographic errors and the variations between the samples are significant. However, a more controlled fabrication processes can eliminate these errors and improve device operation. While an attempt was made to quantify the nonlinear photothermal effect, more experiments and analysis are required to exploit nonlinear phenomenon in silicon waveguides.

5.2   Outlook

As a future scope of this work, some areas that may be looked into are listed below.

1. Performance of VOA may be improved by optimizing diode doping parameters. Higher injection can be achieved by increasing doping concentration and also by reducing junction depth.

2. Modeling of two photon absorption and surface state absorption based detection for wafer scale characterization of photonic devices.

3. Integration of feedback control for stabilization of resonant circuits as shown in the Figure 5.1.
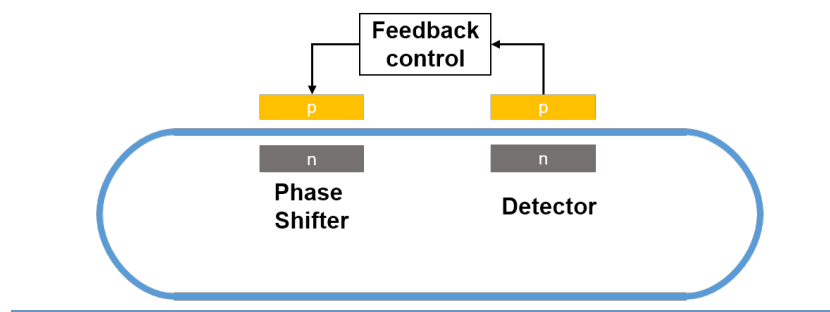
Figure 5.1: Integration of feedback control for a micro ring resonator with two p-i-n diodes

4. Waveguide geometry can be scaled down to sub-micron dimensions where optical mode is tightly confined and is necessary for compact integrated photonic circuit.

APPENDIX A

Chemical Recipes

A.1 RCA-1 and RCA-2 cleaning

RCA-1 is a solution of DI water, aqueous ammonium hydroxide and aqueous hydrogen peroxide in the ratio 5:1:1. Silicon sample is boiled in this solution for about 15 minutes at 80 ° C. This removes organic residues and metallic contaminants and also forms thin layer of silicon dioxide.

RCA-2 is a solution of DI water, aqueous hydrochloric acid and aqueous hydrogen peroxide in the ratio 6:1:1. Silicon sample is boiled in this solution for about 15 minutes at 80 ° C. This removes residual metallic contaminants which were not removed by RCA-1 cleaning and also forms thin layer of silicon dioxide.

In between RCA-1 and RCA-2 clean, an oxide etching step is performed with mixture of hydrofluoric acid and DI water (1:100) and sample is rinsed in DI water and dried using compressed nitrogen.

A.2 Chromium Etchant

Chromium Etchant is a solution prepared from Ammonium Ceric Nitrate (ACN) crystals and acetic acid. It can be prepared as given in the following steps

1. 8g of ACN crystals are fully dissolved in 30ml of DI water

2. 3ml of Acetic acid is dissolved in 35ml of DI water

3. Solutions prepared in the above two steps are mixed and DI water is added in the ratio of 2:1

APPENDIX B

Sheet resistance datasheet for Phosphorous and Boron diffusion

B.1   Phosphorous Diffusion

Details of the process can be found in the reference [52]
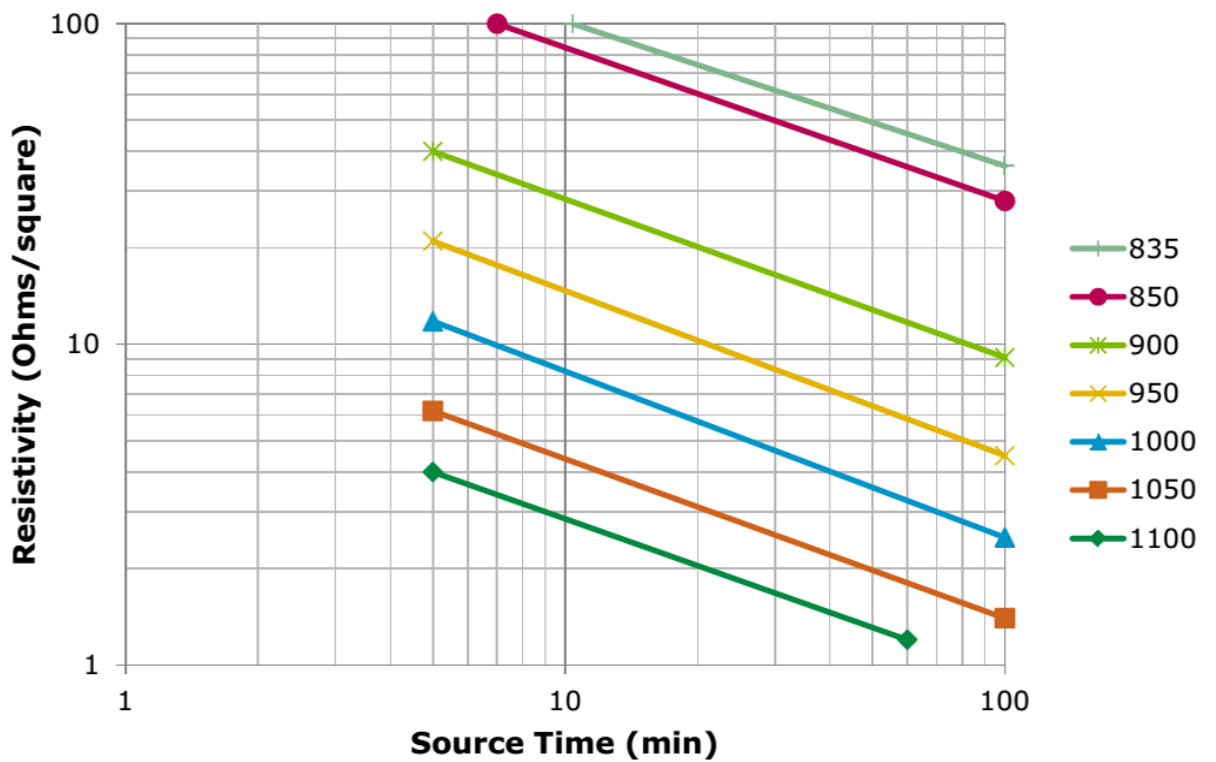
Figure B.1: Sheet resistance data for phosphorous as a function of duration of diffusion

B.2 Boron Diffusion

Details of the process can be found in the reference [54]

Figure B.2: Sheet resistance data for boron as a function of duration of diffusion

REFERENCES

[1] R. Ho, K. W. Mai, M. Horowitz *et al.*, "The future of wires," *Proceedings of the IEEE*, vol. 89, no. 4, pp. 490–504, 2001.

[2] O. Semenov, A. Vassighi, and M. Sachdev, "Impact of self-heating effect on long-term reliability and performance degradation in cmos circuits," *Device and Materials Reliability, IEEE Transactions on*, vol. 6, no. 1, pp. 17–27, 2006.
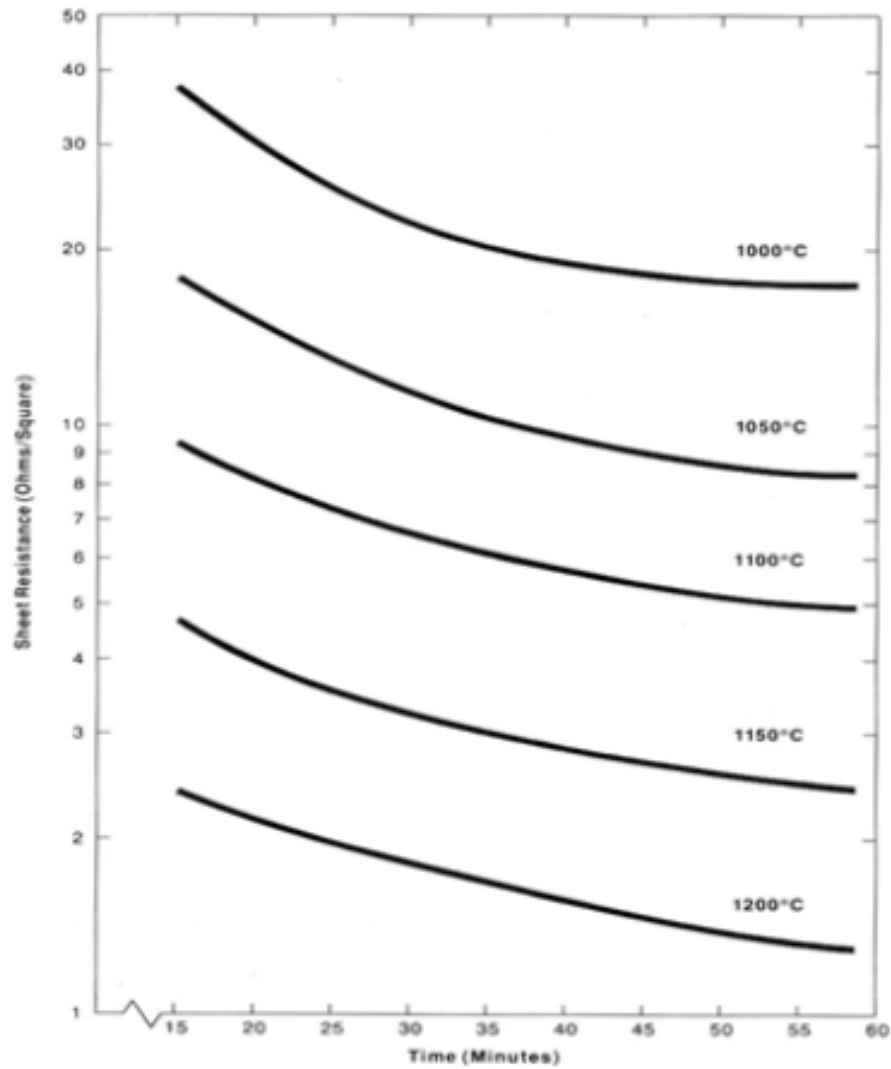
[3] T. Barwicz, H. Byun, F. Gan, C. W. Holzwarth, M. a. Popovic, P. T. Rakich, M. R. Watts, E. P. Ippen, F. X. Kärtner, H. I. Smith, J. S. Orcutt, R. J. Ram, V. Stojanovic, O. O. Olubuyide, J. L. Hoyt, S. Spector, M. Geis, M. Grein, T. Lyszczarz, and J. U. Yoon, "Silicon photonics for compact, energy-efficient interconnects [Invited]," *Journal of Optical Networking*, vol. 6, no. 1, p. 63, 2007.

[4] S. Rumley, D. Nikolova, R. Hendry, Q. Li, D. Calhoun, and K. Bergman, "Silicon photonics for exascale systems," *Journal of Lightwave Technology*, vol. 33, no. 3, pp. 547–562, 2015.

[5] Intel®, *Intel® Silicon Photonics 100G PSM4 Optical Transceiver Brief*, http://www.intel.com/content/www/us/en/architecture-and-technology/silicon-photonics/optical-transceiver-100g-psm4-qsfp28-brief.html, (Accessed: 23 May 2017).

[6] M. Estevez, M. Alvarez, and L. Lechuga, "Integrated optical devices for lab-on-a-chip biosensing applications," *Laser and Photonics Reviews*, vol. 6, no. 4, pp. 463–487, 2012.

[7] C. Doerr, L. Chen, D. Vermeulen, T. Nielsen, S. Azemati, S. Stulz, G. McBrien, X. M. Xu, B. Mikkelsen, M. Givehchi, C. Rasmussen, and S. Y. Park, "Single-chip silicon photonics 100-Gb/s coherent transceiver," *Conference on Optical Fiber Communication, Technical Digest Series*, pp. 7–9, 2014.

[8] G. T. Reed, G. Mashanovich, F. Y. Gardes, and D. J. Thomson, "Silicon optical modulators," *Nature Photonics*, vol. 4, no. 8, pp. 518–526, Jul. 2010.

[9] D.Marris-Morini, R.A.Soref, D.J.Thomson, G.T.Reed, R.K.Schaevitz, and D.A.B.Miller, in *Handbook of Silicon Photonics*. CRC press, 2013, ch. 9, pp. 439–478.

[10] J. Wang, W. Y. Loh, K. T. Chua, H. Zang, Y. Z. Xiong, T. H. Loh, M. B. Yu, S. J. Lee, G. Q. Lo, and D. L. Kwong, "Evanescent-coupled ge p-i-n photodetectors on si-waveguide with seg-ge and comparative study of lateral and vertical p-i-n configurations," *IEEE Electron Device Letters*, vol. 29, no. 5, pp. 445–448, May 2008.

[11] M. W. Geis, S. J. Spector, M. E. Grein, R. T. Schulein, J. U. Yoon, D. M. Lennon, S. Deneault, F. Gan, F. X. Kaertner, and T. M. Lyszczarz, "CMOS-compatible all-Si high-speed waveguide photodiodes with high responsivity in near-infrared communication band," *IEEE Photonics Technology Letters*, vol. 19, no. 3, pp. 152–154, 2007.

[12] Y. Liu, C. W. Chow, W. Y. Cheung, and H. K. Tsang, "In-line channel power monitor based on helium ion implantation in silicon-on-insulator waveguides," *IEEE Photonics Technology Letters*, vol. 18, no. 17, pp. 1882–1884, Sept 2006.

[13] Y. Li and A. W. Poon, "Characterization of surface-state absorption in foundry-fabricated silicon ridge waveguides at 1550 nm using photocurrents," in *Conference on Lasers and Electro-Optics*. Optical Society of America, 2016, p. SM2G.4.

[14] T. Liang and H. Tsang, "Role of free carriers from two-photon absorption in raman amplification in silicon-on-insulator waveguides," *Applied physics letters*, vol. 84, no. 15, pp. 2745–2747, 2004.

[15] R. Claps, V. Raghunathan, D. Dimitropoulos, and B. Jalali, "Influence of nonlinear absorption on raman amplification in silicon waveguides," *Optics Express*, vol. 12, no. 12, pp. 2774–2780, 2004.

[16] S. Abdollahi and M. K. Moravvej-Farshi, "Effects of heat induced by two-photon absorption and free-carrier absorption in silicon-on-insulator nanowaveguides operating as all-optical wavelength converters." *Applied optics*, vol. 48, no. 13, pp. 2505–14, 2009.

[17] Q. Lin, J. Zhang, P. M. Fauchet, and G. P. Agrawal, "Ultrabroadband parametric generation and wavelength conversion in silicon waveguides," *Opt. Express*, vol. 14, no. 11, pp. 4786–4799, 2006.

[18] H. Rong, R. Jones, A. Liu, O. Cohen, D. Hak, A. Fang, and M. Paniccia, "A continuous-wave raman silicon laser," *Nature*, vol. 433, no. 7027, pp. 725–728, 2005.

[19] J. R. Ong, R. Kumar, R. Aguinaldo, and S. Mookherjea, "Efficient CW four-wave mixing in silicon-on-insulator micro-rings with active carrier removal," *IEEE Photonics Technology Letters*, vol. 25, no. 17, pp. 1699–1702, 2013.

[20] S. Fathpour and B. Jalali, "Energy harvesting in silicon optical modulators," *Optics Express*, vol. 14, no. 22, pp. 10 795–10 799, oct 2006.

[21] S. Fathpour, K. K. Tsia, and B. Jalali, "Two-photon photovoltaic effect in silicon," *IEEE Journal of Quantum Electronics*, vol. 43, no. 12, pp. 1211–1217, 2007.

[22] X. Sanga, E. K. Tienb, and O. Boyraz, "Applications of two-photon absorption in silicon," pp. 15–25, 2009.

[23] E.-K. Tien, F. Qian, N. S. Yuksek, and O. Boyraz, "Influence of nonlinear loss competition on pulse compression and nonlinear optics in silicon," *Applied Physics Letters*, vol. 91, no. 20, p. 201115, 2007.

[24] E.-K. Tien, N. S. Yuksek, F. Qian, and O. Boyraz, "Pulse compression and mod-elocking by using tpa in silicon waveguides," *Optics express*, vol. 15, no. 10, pp. 6500–6506, 2007.

[25] O. Boyraz, "Pulse shaping and applications of two-photon absorption," in *Silicon Photonics for Telecommunications and Biomedicine*. CRC Press, 2011, pp. 107–130.

[26] T. Liang, L. Nunes, T. Sakamoto, K. Sasagawa, T. Kawanishi, M. Tsuchiya, G. Priem, D. V. Thourhout, P. Dumon, R. Baets, and H. Tsang, "Ultrafast all-optical switching by cross-absorption modulation in silicon wire waveguides," *Opt. Express*, vol. 13, no. 19, pp. 7298–7303, Sep 2005.

[27] D. J. Moss, L. Fu, I. Littler, and B. Eggleton, "Ultrafast all-optical modulation via two-photon absorption in silicon-on-insulator waveguides," *Electronics letters*, vol. 41, no. 6, pp. 320–321, 2005.

[28] T. Liang, L. Nunes, M. Tsuchiya, K. Abedin, T. Miyazaki, D. Van Thourhout, W. Bogaerts, P. Dumon, R. Baets, and H. Tsang, "High speed logic gate using two-photon absorption in silicon waveguides," *Optics Communications*, vol. 265, no. 1, pp. 171–174, 2006.

[29] Q. Xu and M. Lipson, "All-optical logic based on silicon micro-ring resonators," *Optics express*, vol. 15, no. 3, pp. 924–929, 2007.

[30] T. Liang, H. Tsang, I. Day, J. Drake, A. Knights, and M. Asghari, "Silicon waveg-uide two-photon absorption detector at 1.5 μm wavelength for autocorrelation measurements," *Applied Physics Letters*, vol. 81, no. 7, pp. 1323–1325, 2002.

[31] K. Kikuchi, "Highly sensitive interferometric autocorrelator using Si avalanche photodiode as two-photon absorber," in *Electronics Letters*, vol. 34, no. 1. Opt. Soc. America, 1998, pp. 123–125.

[32] S. P. Group and I. Science, "Optical autocorrelation performance of silicon wire p-i-n waveguides utilizing the enhanced two-photon absorption," vol. 24, no. 26, pp. 29 452–29 458, 2016.

[33] R. Salem, G. Tudury, T. Horton, G. Carter, and T. Murphy, "Polarization-insensitive optical clock recovery at 80 gb/s using a silicon photodiode," *IEEE photonics technology letters*, vol. 17, no. 9, pp. 1968–1970, 2005.

[34] R. Salem, A. A. Ahmadi, G. E. Tudury, G. M. Carter, and T. E. Murphy, "Two-photon absorption for optical clock recovery in otdm networks," *Journal of light-wave technology*, vol. 24, no. 9, p. 3353, 2006.

[35] T. Inui, K. Mori, T. Ohara, H. Takara, T. Komukai, and T. Morioka, "160 gbit/s adaptive dispersion equaliser using asynchronous chirp monitor with balanced dis-persion configuration," *Electronics Letters*, vol. 40, no. 4, pp. 256–257, 2004.

[36] S. Wielandy, P. Westbrook, M. Fishteyn, P. Reyes, W. Schairer, H. Rohde, and G. Lehmann, "Demonstration of automatic dispersion control for 160 gbit/s trans-mission over 275 km of deployed fibre," *Electronics Letters*, vol. 40, no. 11, pp. 690–691, 2004.

[37] I.-W. Hsieh, H. Rong, and M. Paniccia, "Two-photon-absorption-based optical power monitor in silicon rib waveguides," in *7th IEEE International Conference on Group IV Photonics*, 2010.

[38] P. Dong, L. Chen, and Y. kai Chen, "Monolithically integrated voa-mux with power monitors based on submicron silicon photonics platform," in *Optical Fiber Communication Conference*. Optical Society of America, 2012, p. OTu2I.5.

[39] P. Sakthivel, "Design and fabrication of diffusion doped pin waveguides for silicon photonics," Master's thesis, Indian Institute of Technology Madras, Department of Electrical Engineering, Chennai, 2015.

[40] D. Feng, B. J. Luff, and M. Asghari, "Recent advances in manufactured silicon photonics integrated circuits," pp. 826 507–826 507–9, 2012.

[41] D. Feng, J. Luff, S. Jatar, and M. Asghari, "Micron-scale silicon photonic devices and circuits," in *Optical Fiber Communication Conference*. Optical Society of America, 2014, pp. Th4C–1.

[42] A. Martin, J. Luff, D. Feng, and M. Asghari, "Technical Challenges for 100Gb / s Silicon Photonics Transceivers for Data Center Applications," *Optical Fiber Communication Conference 2016*, vol. 1, no. d, pp. 1–3, 2016.

[43] LinkX®-Mellanox Technologies, *LinkX® Variable Optical Attenuators* , http://www.mellanox.com/products/interconnect/variable-optical-attenuators.php, (Accessed: 07 June 2017).

[44] LinkX®-Mellanox Technologies, *LinkX® Ethernet Optical Transceivers* , http://www.mellanox.com/products/interconnect/ethernet-optical-transceivers.php, (Accessed: 07 June 2017).

[45] Lumerical, "MODE," https://www.lumerical.com/tcad-products/mode/, (Accessed: 21 May 2017).

[46] R. Soref and B. R. Bennett, "Kramers-kronig analysis of electro- optical switching in silicon," *Proc. SPIE*, vol. 704, pp. 32–37, 1986.

[47] Lumerical, "DEVICE," https://www.lumerical.com/tcad-products/device/, (Accessed: 19 April 2017).

[48] D. Dimitropoulos, R. Jhaveri, R. Claps, J. C. S. Woo, and B. Jalali, "Lifetime of photogenerated carriers in silicon-on-insulator rib waveguides," *Applied Physics Letters*, vol. 86, no. 7, p. 071115, 2005.

[49] D. W. Zheng, B. T. Smith, and M. Asghari, "Efficient silicon-photonic modulator with recessed electrodes," vol. 6898, 2008, p. 68980A.

[50] J. Plummer, *Silicon VLSI Technology: Fundamentals, Practice and Modeling*. Pearson Education, 2009.

[51] S. Ghandhi, *VLSI Fabrication Pinciples: Silicon AND Gallium Arsenide, 2nd Ed.* Wiley India Pvt. Limited, 2008.

[52] *Process Guidelines for Using Phosphorous Oxychloride as an N-Type Silicon Dopant*, Air Products and Chemicals, Inc., 2015.

[53] *PDS® Products P-Type Planar Diffusion Sources , Low Temperature Oxiation and Silicon-Boron (Si-B) Layer*, Saint-Gobain, 2014.

[54] *PDS® Products P-Type Planar Diffusion Sources (Product Datasheet)*, Saint-Gobain, 2014.

[55] G. Reed and A. Knights, *Silicon Photonics: An Introduction*.

[56] Z. Wang, H. Liu, Q. Sun, N. Huang, S. Li, and J. Han, "The influence of thermal and free carrier dispersion effects on all-optical wavelength conversion in a silicon racetrack-shaped microring resonator," *Laser Physics*, vol. 26, no. 7, p. 075403, 2016.

[57] A. Yariv and P. Yeh, *Photonics: Optical Electronics in Modern Communications*. Oxford University Press, 2006.

LIST OF PUBLICATIONS

Papers in Conferences

1. Sreevatsa Kurudi and Bijoy Krishna Das, "Design and Demonstration of Polarization Independent Variable Optical Attenuator with SOI Waveguides," in 13th International Conference on Fiber Optics and Photonics, OSA Technical Digest (online) (Optical Society of America, 2016), paper W4F.3.

2. Riddhi Nandi, Sreevatsa Kurudi and Bijoy Krishna Das,"Diffusion doped p-i-n/p-n diodes for scalable silicon photonics devices," Proc. SPIE 10249, Integrated Photonics: Materials, Devices, and Applications IV, 102490Q (2017).

Papers in Journal

1. Bijoy Krishna Das, Nandita DasGupta, Sujith Chandran, Sreevatsa Kurudi, et.al, "Silicon Photonics Technology : Ten Years of Research at IIT Madras," Asian Journal of Physics 25(7), 923 – 955 (2016).

2. Sujith Chandran, Meenatchi Sundaram, Sreevatsa Kurudi, and Bijoy Krishna Das, "Design and fabrication of surface trimmed silicon-on-insulator waveguide with adiabatic spot-size converters," Appl. Opt. 56, 1708-1716 (2017).

GENERAL TEST COMITTEE

CHAIR PERSON : Dr. Harishankar Ramachandran

                     Professor

                     Department of Electrical Engineering

                     Indian Institute of Technology, Madras

GUIDE : Dr. Bijoy Krishna Das

                     Associate Professor

                     Department of Electrical Engineering

                     Indian Institute of Technology, Madras

MEMBERS : Dr. Deleep R Nair

                     Assistant Professor

                     Department of Electrical Engineering

                     Indian Institute of Technology, Madras

  : Dr. Manu Jaiswal

                     Assistant Professor

                     Department of Physics

                     Indian Institute of Technology, Madras